

A Sensitivity Analysis of the Anisotropy of Hydraulic Conductivity to the Seepage, Deformation and Stability of Anti-Dipping Layered Rock Slopes: A Case Study of the Pulang Area in Southwestern China

Guangkeng Zhang

Central South University

Guangyin Lu (✉ luguangyin@csu.edu.cn)

Central South University

Chengzhi Xia

Central South University

Lianrong Wu

Central South University

Zongming Xu

Central South University

Ying Bai

Central South University

Jialu Li

Central South University

Original Paper

Keywords: anisotropy of hydraulic conductivity, anti-dipping layered rock slopes, anisotropy ratios, anisotropy angles, numerical simulations

Posted Date: February 9th, 2021

DOI: <https://doi.org/10.21203/rs.3.rs-172431/v1>

License: © ⓘ This work is licensed under a Creative Commons Attribution 4.0 International License.

[Read Full License](#)

Version of Record: A version of this preprint was published at Geotechnical and Geological Engineering on June 25th, 2021. See the published version at <https://doi.org/10.1007/s10706-021-01910-z>.

1 **Geotechnical and Geological Engineering**
2 **A Sensitivity Analysis of the Anisotropy of Hydraulic**
3 **Conductivity to the Seepage, Deformation and Stability of Anti-**
4 **Dipping Layered Rock Slopes: A Case Study of the Pulang Area**
5 **in Southwestern China**

6 Guangkeng Zhang^{1,2,3} · Guangyin Lu^{1,2,3} · Chengzhi Xia^{1,2,3} · Lianrong Wu⁴ · Zongming Xu⁵ · Ying
7 Bai⁵ · Jialu Li^{2,3}

8 ¹ School of Geosciences and Info-Physics, Central South University, Changsha 410083, China;
9 zgk2019@csu.edu.cn (Guangkeng Zhang); xiachengzhi@csu.edu.cn (Chengzhi Xia)

10 ² Key Laboratory of Metallogenic Prediction of Nonferrous Metals and Geological Environment Monitoring
11 Ministry of Education, Central South University, Changsha 410083, China; dj195011068@csu.edu.cn (Jialu Li)

12 ³ Hunan Key Laboratory of Nonferrous Resources and Geological Hazards Exploration, Changsha 410083, China

13 ⁴ Yunnan Diquing Nonferrous Metals Co., Ltd., Diquing 474400, China; keliang_shi@csu.edu.cn (Lianrong Wu)

14 ⁵ China Nonferrous Metals Industry Kunming Survey, Design and Research Institute Co., Ltd. Experimental
15 Center, Kunming 650000, China; 195011071@csu.edu.cn (Zongming Xu); 0110160309@csu.edu.cn (Ying Bai)

16 Correspondence should be addressed to Guangyin Lu; luguangyin@csu.edu.cn

17 **Abstract**

18 In this paper, in order to study the influencing effects of anisotropy ratios and anisotropy directions on the seepage,
19 deformations and stability of the anti-dipping layered rock slopes, Geo-studio software was used in this study to
20 carry out this test based on the unsaturated seepage, fluid-solid coupling, and stability theory numerical analysis
21 of carbonaceous slate slopes in Pulang area. The results showed that the maximum surface water content of the
22 layered rock slopes gradually decreased with increases of the water conductivity anisotropy ratio and decreases
23 in the anisotropy angle of the anti-dipping layered rock slopes. In addition, the rainfall infiltration depths in the
24 middle sections of the slopes were observed to be the most affected by the anisotropy ratio and dip angles of the
25 rock formations. Meanwhile, the bottom sections of slopes were the least affected by the anisotropy ratio and the
26 dip angles of the rock formations. In regard to the anti-dipping rock slopes, it was found that the anisotropy ratio
27 and rock layer dip angles should be considered in the deformation and stability analyses. When the seepage of an
28 anti-dipping layered slope was considered to be isotropic, the safety factors often were overestimated. As the
29 anisotropy ratio decreases and the anti-tilt angles of the layered planes increases, the safety factors of the slopes
30 will gradually decrease. This study provided a feasible scheme for evaluating the seepage, deformations and
31 stability of the anti-dipping layered rock slopes in southwest China's Pulang area.

32 **Keywords:** anisotropy of hydraulic conductivity · anti-dipping layered rock slopes · anisotropy ratios · anisotropy
33 angles · numerical simulations

35 **1 Introduction**

36 In addition to earthquakes and volcanic eruptions, landslides are one of the three major global geological
37 disasters. Landslides caused by slope instability have always been important subjects in geotechnical engineering.
38 As shown in Table 1, some of China's major landslide events have resulted in significant economic losses. There
39 are many factors which are known to cause landslides, such as heavy rainfall, earthquakes, and reservoir storage
40 processes (Iverson 2000; Zhong et al. 2007). In recent years, more than 80% of China's landslide disasters
41 occurred in the months of May to September when rainfall was abundant, with more than 90% of the landslides
42 induced by heavy rainfall (Zhang et al. 2005). The main reasons for the landslides caused by rainfall are as follows:
43 (1) Rainfall reduces the matrix suction of rock slopes, thereby reducing the effective stress and shear strength of

44 rock masses; (2) Heavy rainfall increases the horizontal displacements of slopes and aggravates the instability of
 45 the slopes. Rainfall-induced landslides have posed severe threats to China, as well as other countries throughout
 46 the world, by severely restricting the economic development of landslide disaster areas and threatening the lives
 47 and property of the majority of people in those affected regions. For example, in August of 2013, southern China
 48 underwent heavy rains, and landslides occurred along the railway system from Chenzhou, Hunan to Shaoguan,
 49 Guangdong. The railway transportation system was severely blocked, causing about 20,000 passengers to be
 50 stranded at the Guangzhou Railway Station. In July of 2019, an extremely large landslide occurred in the Chagou
 51 Group of Pingdi Village, located in Jicang Town, Shuicheng County, Liupanshui City, Guizhou Province. The
 52 disaster resulted in the deaths of 51 people. The data monitored by the Meteorological Department showed that
 53 the incident was concentrated in the region which had experienced recent heavy rainfall (Liu et al. 2010). From
 54 the above-mentioned examples, it can be seen that slope instability damages are closely related to heavy rainfall
 55 events. Therefore, deepening the understanding the mechanism of rainfall infiltration will potentially be of major
 56 significance in future measures implemented for the prevention and control of landslide disasters.

57 **Table 1** Landslide disasters in China recent years

Landslide site	The number of casualties	Property loss
Shenzhen Guangming	77 people were killed	880 million yuan
Shanyang County	65 people were killed	500 million yuan
Tibet Yigong	96 people were killed	420 million yuan
Ganjiangping	24 people were killed	57.35 million yuan
Sichuan Wangjiayan	1,700 people were killed	16 million yuan
Guizhou Shuicheng	52 people were killed	190 million yuan

58 At the present time, the numerical simulations of rainfall-induced landslides are a hot issues. Many
 59 researchers have conducted studies regarding the mechanisms of rainfall infiltration. A large number of conceptual
 60 infiltration models and numerical simulations have been applied in order to examine rainfall-induced landslides.
 61 Based on Darcy's Law and rainwater infiltration quality conservation equations, Zhang Jie et al. (2014)
 62 established an infiltration layering hypothesis based on the change characteristics of loess infiltration profiles.
 63 Subsequently, the relationships between the infiltration depths and the time factors were derived, which were used
 64 to calculate the slope safety factors. Gan Yongde et al. (2015) introduced saturation coefficients for the purpose
 65 of quantifying the influencing effects of air resistance and established a Green-Ampt Model which considered the
 66 effects of air resistance under unsteady rainfall conditions. In terms of numerical simulations, Yang Pan and Yang
 67 Jun (2015) used the geotechnical finite element software Plaxis to consider rainfall infiltration and the properties
 68 of unsaturated soils, and then studied and analyzed landslide early warning rainfall thresholds. Some researchs,
 69 such as Kulatilake (2001), Zhou Weiyuan (1990), Yang (1998), Zhu Weishen (1994) and so on constructed rock
 70 mass models and numerical models using gypsum, yellow sand and other materials, for the purpose of
 71 investigating the anisotropic modes and seepage characteristics of rock masses.

72 However, this study observed that the majority of the previous related studies had regarded slope materials
 73 as isotropic materials. Song et al. (2018) conducted experiments regarding clay layers along horizontal and vertical
 74 directions in order to study the permeability coefficient and anisotropy of the shallow clay in Shanghai. The results
 75 revealed that the flocculent microstructures formed by sedimentation displayed large differences in the vertical
 76 and horizontal permeability coefficients. Lee (2020) conducted penetration experiments on sedimentary rock and
 77 determined that the ratio of the parallel/perpendicular to the bedding plane was 10-100. Ning Shuai et al. (2021)
 78 considered the anisotropy in slope stability analyses and found that when considering the anisotropy condition,
 79 the anisotropy was generally less than the safety factors under isotropic conditions. However, none of the above-
 80 mentioned studies considered the anisotropy angles of hydraulic conductivity. Yu et al. (2020) performed
 81 numerical simulations of the permeability and stability of sandy clay. The results indicated that only under special
 82 circumstances, the horizontal permeability coefficient and the vertical permeability coefficient coincide with the
 83 natural coordinate axis. It has been observed that the anisotropy direction does not coincide with the coordinate
 84 axis in most situations. In recent years, researchs in the field have paid increasing amounts of attention to anti-
 85 dipping slopes. Su et al. (2012) established a typical anti-dipping rock slope model using the FINAL system and
 86 studied the failure mechanisms of this type of rock slope with different bedding dip angles. Yao Ye et al. (2020)
 87 studied the mechanisms of the deformations and failures of anti-dipping cataclastic structure rock slopes in
 88 southwestern China using various experimental processes and successfully obtained the failure mechanisms of
 89 anti-dipping layered rock slopes. Cheng et al. (2019) revealed the impacts of steep anti-dipping sandstone in
 90 mudstone slopes. Zhu et al. (2020) found that the failure mechanisms of anti-dipping layered slopes were
 91 essentially different from those of bedding slopes. Huang et al. [20] proposed a stability evaluation method for

92 anti-dipping rock slopes and revealed the failure characteristics of landslides under different inclination angles.
 93 Tao et al. (2020) determined the failure modes of the Changshanhao gold mine slopes using field experiments and
 94 put forward suggestions for the reinforcement and treatment of dangerous slopes. Liu et al. (2020) selected the
 95 Diaokanlong Tunnel of the Rucheng-Chenzhou Expressway in central China as an example and analysed the
 96 deformation characteristics and evolution processes of the anti-dipping slope failure through field investigation,
 97 deformation monitoring and numerical analysis. However, the current research studies regarding anti-dipping
 98 layered rock slopes have focused on the failure mechanisms and there have been few studies completed regarding
 99 the seepage characteristics, deformations and stability levels of anti-dipping rock slopes.

100 In view of the shortcomings of the previous studies, this research investigation first described the
 101 mathematical definition of the anisotropy ratio and direction of hydraulic conductivity. Taking the strongly
 102 weathered anti-dipping layered rock slopes in the Pulang area of Yunnan, China as an example, the unsaturated
 103 seepage simulation was realized by the Van Genuchten and fluid-soil coupling theory. Then, the layered rock
 104 body water retention curves were obtained and a reasonable initial matrix suction was successfully determined.
 105 Finally, according to the volumetric water content, maximum surface water content (MWCS); rainfall infiltration
 106 depth (RID); maximum horizontal displacement (MHD) and the safety factor (SF) of three typical anti-incline
 107 slopes (top, middle and bottom), the effects of different anisotropy ratios and anisotropy angles on the permeability
 108 sensitivity, deformations and stability levels of anti-dipping layered rock slopes were discussed. The feasibility
 109 of this study's numerical simulations were confirmed using the field survey data. The research results provided
 110 important references for deepening understanding of anisotropy of hydraulic conductivity and landslide
 111 prevention.

112 2 Methods and Theory

113 2.1 Control differential equation

114 In this study, the SWEEP/W module in Geo-studio was used to simulate the seepage processes of the slopes.
 115 The rainfall infiltration vales were used as the variable flow boundaries of the unsaturated zones for the numerical
 116 simulations. According to the principle of conservation of mass, the saturated-unsaturated seepage control
 117 equation (SEEP/W 2007) was as follows:

$$118 \quad \frac{\partial}{\partial x} \left(k_x \frac{\partial H}{\partial x} \right) + \frac{\partial}{\partial y} \left(k_y \frac{\partial H}{\partial y} \right) + Q = m_w \gamma_w \frac{\partial H}{\partial t} \quad (1)$$

119 Where x and y are the coordinates in the direction of x and y ; H is the total head, and the unit is m; k_x represents
 120 the hydraulic conductivity in the x -direction, and the unit is m/s; k_y indicates the hydraulic conductivity in the y -
 121 direction, and the unit is m/s; Q represents the applied boundary flux, in which m_w is the slope of the storage
 122 curve; t is the time, and the unit is s; γ_w denotes the unit weight of the water, and the unit is N/m³.

123 2.2 Fluid-structure interactions

124 In this study, when solving the rock and soil deformations of slopes, a fluid-structure interaction theory was
 125 adopted. Meanwhile, the seepage and rock and soil deformations were solved simultaneously. The finite element
 126 equilibrium equation could then be expressed by the virtual work principle in the Geo-studio SIGMA / W system,
 127 which indicated that the total internal virtual work was equal to the external virtual work. In simple cases, when
 128 only the external point load $\{F\}$ is applied, the virtual work equation can be written as follows:

$$129 \quad \int \{\varepsilon^*\}^T \{\Delta\sigma\} dV = \int \{\delta^*\}^T \{F\} dV \quad (2)$$

130 Where $\{\delta^*\}$ indicates the virtual displacement; $\{\varepsilon^*\}$ denotes the virtual strain; and $\{\sigma\}$ is the internal stress.
 131 Therefore, the two-dimensional seepage flowing through a unit of soil can be expressed by the Darcy Equation as
 132 follows:

$$133 \quad \frac{k_x}{\gamma_w} \frac{\partial^2 u_w}{\partial x^2} + \frac{k_y}{\gamma_w} \frac{\partial^2 u_w}{\partial y^2} + \frac{\partial \theta_w}{\partial t} = 0 \quad (3)$$

134 Where k_x and k_y represent the hydraulic conduction coefficients in the x and y directions, respectively; u_w is the
 135 seepage velocity; γ_w indicates the unit weight of the water; θ_w is the volumetric water content; and t denotes the

136 time. The volumetric water content of elastic materials may be expressed by the following equation
 137 (Dakshanamurthy and Rahardjo 1984):

$$138 \quad \left. \begin{aligned} \beta &= \frac{E}{H} \frac{1}{(1-2\nu)} = \frac{3K_B}{H} \\ \omega &= \frac{1}{R} - \frac{3\beta}{H} \end{aligned} \right\} \quad (4)$$

139 Where K_B indicates the bulk modulus; and R is the modulus related to volumetric water content as a function of
 140 the matrix suction. Then, by inputting equation (3) into equation (2), numerical integration can be performed. The
 141 finite element equation solved by SIGMA / W can then be expressed by the following equations:

$$142 \quad \Sigma [B]^T [D] [B] \{\Delta\delta\} + \Sigma [B]^T [D] [B] \{m_H\} \langle N \rangle \{\Delta u_w\} = \Sigma F \quad (5a)$$

$$143 \quad [K] = [B]^T [D] [B] \quad (5b)$$

$$144 \quad [L_d] = [B]^T [D] \{m_H\} \langle N \rangle \quad (5c)$$

$$145 \quad \{m_H\}^T = \left\langle \frac{1}{H} \frac{1}{H} \frac{1}{H} \right\rangle 0 \quad (5d)$$

146 Where $[B]$ represents the gradient matrix; $[D]$ is the constitutive matrix for the drainage; $[K]$ indicates the stiffness
 147 matrix; $[L_d]$ denotes the coupling matrix; $\{\Delta\delta\}$ is the incremental displacement vector; and Δu_w represents the
 148 incremental pore water pressure (PWP) vector.

149 2.3 Safety factors of unsaturated layered rock slopes

150 In this study, the Morgenstern-Price Method, which is based on a limit equilibrium theory was used to
 151 calculate the safety factors of the slopes. The aforementioned method has the ability determine the relevant
 152 parameters more accurately by studying the sliding surfaces of rock landslides under the limit equilibrium state,
 153 thereby providing a reliable basis for the analysis and design of landslide engineering (Morgenstern and Price
 154 1965). Therefore, it was considered to be reasonable to use the Morgenstern-Price Method for this study's slope
 155 stability analysis (Xiao and Li 2020). In addition, the improved method satisfied both the force balance and torque
 156 balance requirements, and the calculation accuracy was observed to be higher.

157 This study selects a rock slice as the research object, as shown in Fig. 1. According to the balance of the
 158 force in the normal and tangential directions of the slip surfaces of the rock slice, when the boundary conditions
 159 were $E_o = 0$ and $E_n = 0$, the following was obtained:

$$160 \quad S_i = (N_i \tan \varphi + cb \sec \alpha) / F_s \quad (6)$$

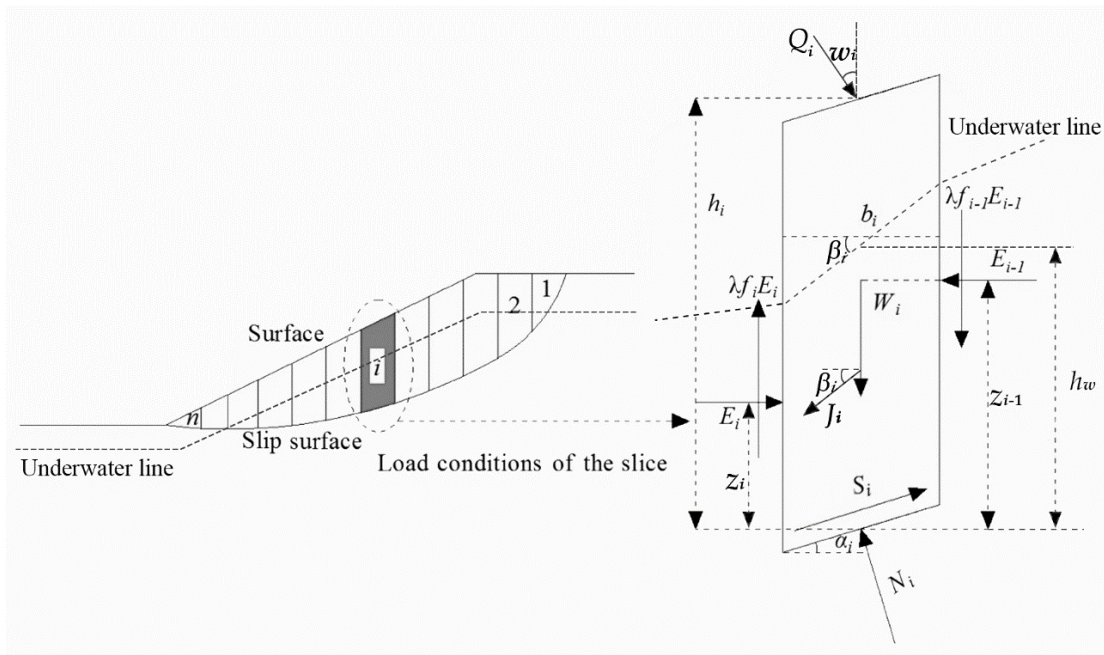
$$161 \quad N_i = (W_i + \lambda f_{i-1} E_{i-1} - \lambda f_i E_i + Q_i \cos \omega_i + J_i \sin \beta_i) \cos \alpha + E_i - E_{i-1} + Q_i \sin \omega_i - J_i \cos \beta_i \sin \alpha_i \quad (7)$$

162 Where N_i is the effective normal force on the slip surfaces of the rock slice and the unit is kN; S_i indicates the
 163 shear force on the slip surfaces of the rock slice and the unit is kN and the safety factor F_s can be derived as
 164 follows:

$$165 \quad F_s = \frac{\sum_{i=1}^{n-1} (R_i \prod_{j=i}^{n-1} \psi_j) + R_n}{\sum_{i=1}^{n-1} (T_i \prod_{j=i}^{n-1} \psi_j) + T_n} \quad (8)$$

166 Where R_i is the resistance force, $R_i = [W_i \cos \alpha_i + Q_i \cos(\omega_i - \alpha_i) + J_i \sin(\beta_i - \alpha_i)] \tan \varphi_i + c_i b_i \sec \alpha_i$, and the unit
 167 is kPa; T_i is the sliding force, $T_i = W_i \sin \alpha - Q_i \sin(\omega_i - \alpha_i) + J_i \cos(\beta_i - \alpha_i)$; ψ_i denotes the transfer coefficient,

168
$$\psi_{i-1} = \frac{(\sin \alpha_i - \lambda f_{i-1} \cos \alpha_i) \tan \varphi_i + (\cos \alpha_i + \lambda f_{i-1} \sin \alpha_i) F_s}{(\sin \alpha_{i-1} - \lambda f_{i-1} \cos \alpha_{i-1}) \tan \varphi_{i-1} + (\cos \alpha_{i-1} + \lambda f_{i-1} \sin \alpha_{i-1}) F_s}$$
; c_i represents the effective cohesion for
 169 every rock slice and the unit is kPa; φ_i represents the shear strength angle for every rock slice, and the unit is the
 170 degree; J_i is the seepage force of the rock slippage which adopts a simplified seepage field treatment method,
 171 assuming that its position of action is located at the center of the gravity of the rock below the underwater line,
 172 and the distance from the center of the slip surface of the rock strip is $h_w/2$; h_w denotes the distance from the
 173 underwater line to the slip surface; E_i and E_{i-1} are the horizontal effective forces between the two sides of the rock
 174 slices and the unit is kN; $\lambda f_i E_i$ and $\lambda f_{i-1} E_{i-1}$ represent the shear forces between the two sides of the rock strip; f_i is
 175 the function of the inter-strip force; and λ is the proportional coefficient. The distances between the action
 176 positions on both sides and the center of the slip surfaces of the rock strip are denoted as Z_i and Z_{i-1} , respectively;
 177 W_i is divided into two parts based on the underwater line: $W_i = W_{i1} + W_{i2}$, where W_{i1} is the gravity of the rock above
 178 the underwater line and W_{i2} represents the floating weight of the rock below the underwater line; Q_i indicates the
 179 external force on the rock surface; ω_i is the angle between the direction of the external force and the normal
 180 direction; α_i indicates the angle of the slip surface.



181
 182 **Fig. 1** Calculation principle and model of the Morgenstern–Price (M–P) Method

183 **3. Numerical model framework**

184 3.1 Numerical model and boundary conditions

185 The study are examined in this research investigation was an anti-dipping layered rock slope in the Pulang
 186 area located in Yunnan, China. In Fig. 2, I and II represent the strongly weathered carbonaceous slate and
 187 moderately weathered carbonaceous slate in the study area, which were characterized by their bedding structures.
 188 The height of the examined slope was 89 m and the length was 217m. In order to closely examine the strongly
 189 weathered carbonaceous slate, the grid size of the strongly weathered area was set to 1 m, and the grid size of the
 190 moderately weathered area was set as 5 m. The grid model was then divided into 7,057 nodes and 6,960 units. In
 191 order to study the characteristics of different locations, three monitoring lines and three monitoring points were
 192 set at $x = 25$ m (top of the slope), $x = 67$ m (middle of the slope) and $x = 108$ m (bottom of the slope), respectively,
 193 with the monitoring points located on the slope surfaces below 8m. The boundary conditions were as follows: AB
 194 and HF were the fixed water level boundaries of 76 m and 19 m, respectively; CD represented the rainfall
 195 infiltration boundary; BC and GF were the small flow boundaries; AH indicated the impermeable boundary; DE
 196 represented the water level of the tailings reservoir at 36 m. In addition, in order to clearly reflect the real rainfall
 197 situation, the daily rainfall data from March 1st to August 1st of 2019 in the Pulang region were used as the rainfall
 198 conditions, as shown in Fig. 3.

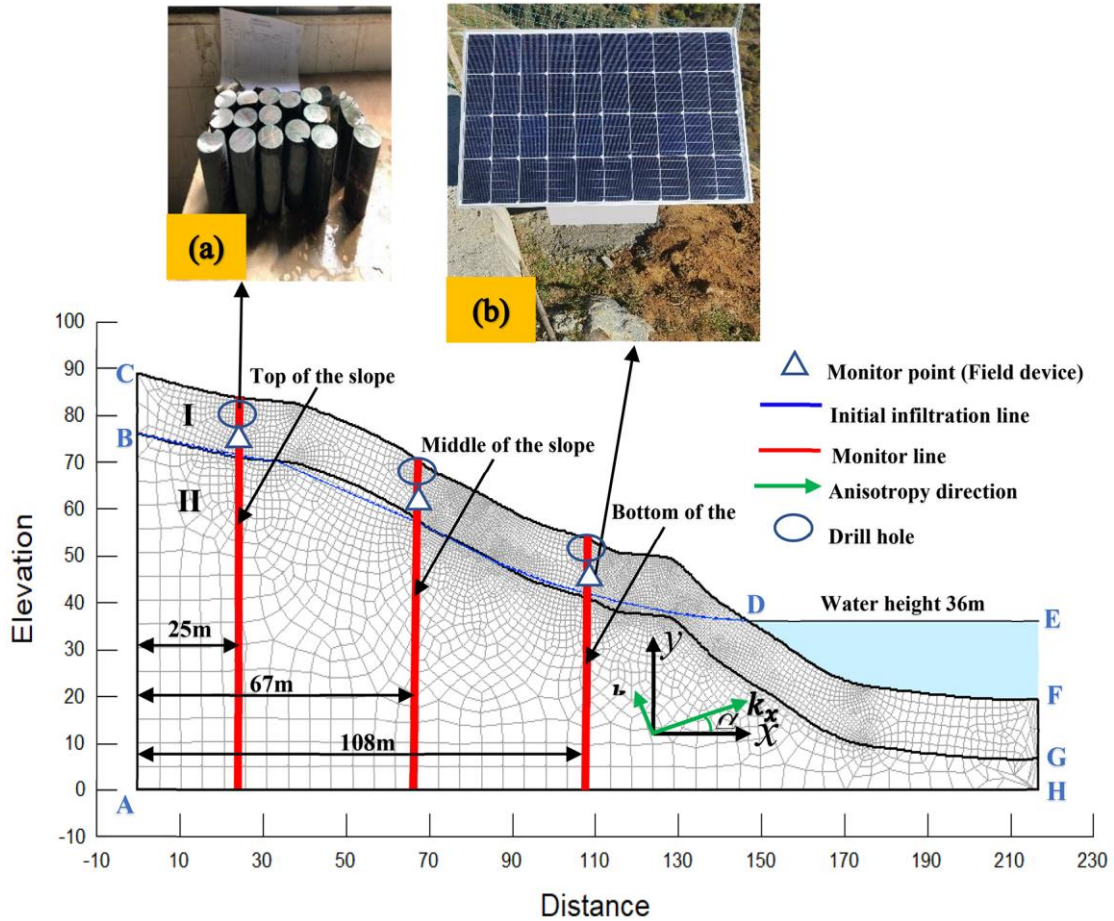


Fig. 2 Grid model

199
200

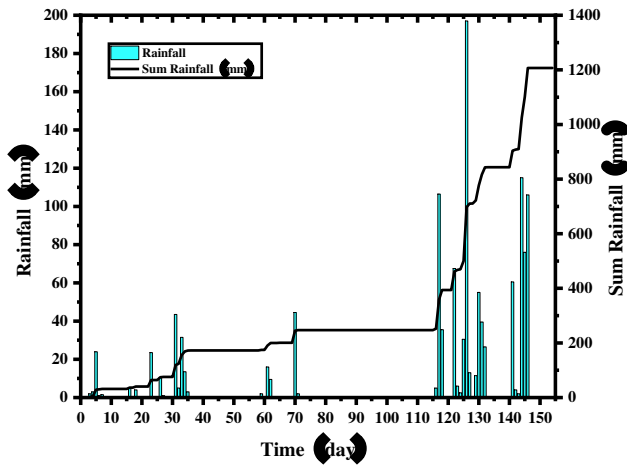


Fig. 3 Daily rainfall values from March 1st to August 1st of 2019

201
202

203 3.2 Analysis of the unsaturated layered rock mass

204 Previous studies have found that in practice, it is difficult to accurately measure the unsaturated characteristic
 205 curves of rock masses. Therefore, the classic water retention curve of unsaturated porous media (Brooks and
 206 Corey 1964; Fredlund and Xing 1994; V Genuchten 1980), along with relative hydraulic conductivity models
 207 (Mualem 1976) are often used to describe fractures and weakly permeable rock formations under unsaturated flow
 208 conditions. Therefore, for the soil-water characteristic curves (SWCC) of this study, the Van Genuchten model
 209 was adopted. The Van Genuchten model is as follows:

210
$$\theta = \theta_r + \frac{\theta_s - \theta_r}{[1 + (p/a)^n]^m} \quad (9)$$

211
$$k = k_w \frac{[1 - |p/a|^{n-1} (1 + |p/a|^n)^{-m}]^2}{(1 + |p/a|^n)^2} \quad (10)$$

212 Where p is the suction, and the unit is kPa; θ indicates the adjusted volumetric water content, and the unit is m^{-1} ;
 213 θ_r represents the residual volumetric water content, and the unit is m^{-1} ; θ_s indicates the saturated volumetric water
 214 content, and the unit is m^{-1} ; a denotes the fitting parameter which is closely related to the air-entry value of the
 215 unsaturated rock mass, and the unit is kPa; n and m ($m = 1 - 1/n$ and $n > 1$) are the fitting parameters which control
 216 the slope at the inflection point in the volumetric water content function [29]; k_w denotes the saturated hydraulic
 217 conductivity, and the unit is m/s; and k indicates the adjusted hydraulic conductivity, and the unit is m/s.

218 Carbonaceous slate was used in this study, as shown in Fig. 4. According to the research of Chen et al.
 219 (2020), the range of the unsaturated fitting parameters of the VG model of the layered rock mass was determined,
 220 and the Geo-studio was used to numerically simulate the slope. It was concluded that the time and location of the
 221 numerical simulation are consistent with the monitoring data. The pore water pressure of the numerical simulation
 222 was compared with the monitoring data, the fitting parameters were determined, and the water retention curve
 223 was obtained (Xia et al. 2020). The water retention curve parameters are shown in Table 2 and the SWCC curves
 224 are detailed in Fig. 5.



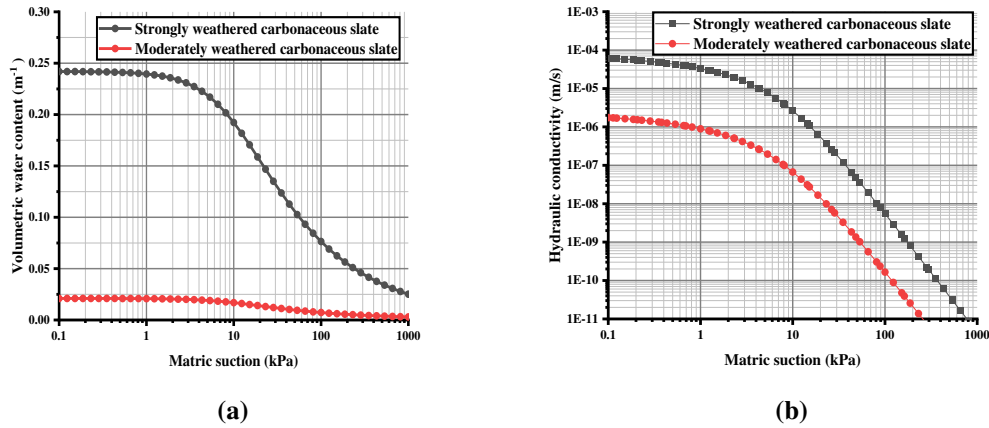
225 **Fig. 4** Images of the carbonaceous slate samples

226 **Table 2** Parameters of the water retention curves

227

Layer	Materials	Fitting parameters					Hydraulic conduction coefficient $k[m/s]$
		A[kPa]	m	n	θ_s	θ_r	
I	Strongly weathered carbonaceous slate	10	0.33	1.5	0.242	0.001	8.08×10^{-5}
II	Moderately weathered carbonaceous slate	10	0.33	1.5	0.021	0.001	2.47×10^{-6}

228



229 **Fig. 5** SWCC curve: **a** Water retention curve; **b** Hydraulic conductivity curve.

230 3.3 Definition and calculation conditions of the anisotropy

231 The previous analysis results revealed that the previous researchs had neglected the anisotropy ratios and
 232 angles in their investigations. However, it is known that anisotropy is widespread in rock masses. In the current
 233 study, the hydraulic conductivity matrix $[C]$ was expressed as follows:

234
$$[C] = \begin{bmatrix} C_{11} & C_{12} \\ C_{21} & C_{22} \end{bmatrix} \quad (11)$$

235 In Equation (11), $C_{11} = k_x \cos^2 a + k_y \sin^2 a$, $C_{22} = k_x \sin^2 a + k_y \cos^2 a$, and $C_{21} = C_{12} = k_x \cos^2 a +$
 236 $k_y \sin^2 a$. The k_y/k_x and the anisotropy direction a were defined according to Fig. 3, where k_x is the horizontal
 237 hydraulic conduction coefficient; k_y is the vertical hydraulic conduction coefficient; and a indicates the direction
 238 between k_x and the x axis. Therefore, when $a = 0^\circ$, $[C]$ is reduced to the following:

239
$$[C] = \begin{bmatrix} k_x & 0 \\ 0 & k_y \end{bmatrix} \quad (12)$$

240 Equation (12) was utilized in the present study, and only the anisotropy ratio $k_r = k_y/k_x$ was considered.
 241 However, the definition of rock mass anisotropy is not only the anisotropy ratio, but also the anisotropy angle.
 242 Therefore, in order to better study the anisotropy of the layered rock masses, including the anisotropy ratio k_r and
 243 the anisotropy direction a , the calculation conditions shown in Table 3 were implemented. Then, by combining
 244 the findings of previous studies (Yao et al. 2020; Cheng et al. 2020; Yu et al. 2020), the anisotropy ratio $k_r = 0.01,$
 245 $0.02, 0.1,$ and 1 and the anisotropy direction $a = 0^\circ, -15^\circ, -30^\circ, -45^\circ, -60^\circ, -75^\circ,$ and -90° were successfully
 246 determined. The failure criterion of the rock mass layered slope simulations adopted the Mohr-Coulomb Criterion,
 247 and the rock mass strength parameters were determined from the geotechnical test results, as detailed in Table 4.

248 **Table 3** Calculation conditions

Rock types	Anisotropy ratio $k_r = k_y/k_x$	Anisotropy angle $a [^\circ]$
Strongly weathered carbonaceous slate	[0.01 0.02 0.1 1]	[0 -15 -30 -45 -60 -75 -90]

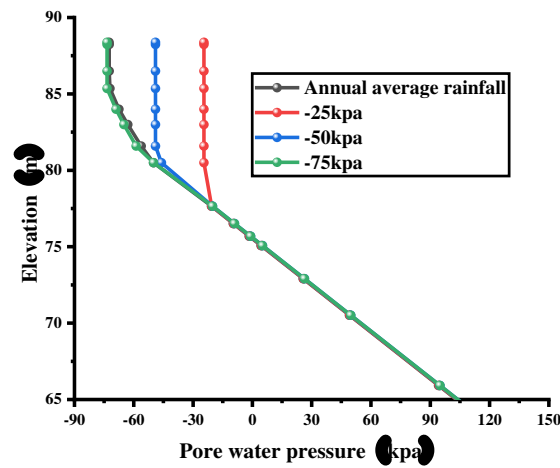
249 **Table 4** Rock mass strength parameters

Rock types	Elastic modulus [Mpa]	Poisson ratio	Unit weight [kN/m ³]	Cohesion [kPa]	Friction angle [°]
Strongly weathered carbonaceous slate	2644.9	0.38	22.4	93.6	33.3
Moderately weathered carbonaceous slate	5561	0.35	26.5	120	35

251 **4. Results and Discussion**

252 4.1 Initial conditions

253 The determination of the initial conditions was very important for the next step of the numerical simulation.
254 In order to make the initial matrix suction more in line with the actual situation, this study calculated the maximum
255 pore water pressure of -25 kpa, -50 kpa, -75 kpa and the annual average rainfall of 0.6 mm/h in the Pulang area.
256 The infiltration volume was numerically simulated and the pore pressure changes in the slate are shown in Fig. 6.
257 It can be seen from the figure that the pore water pressure changes of the average annual rainfall were the closest
258 to a maximum pore water pressure of -75 kpa. Therefore, the initial pore water pressure levels of all this study's
259 simulation experiments were set as -75kpa, which was to be consistent with the actual situation in the Pulang
260 area.



261

262 **Fig. 6** Initial pore pressure distribution

263 4.2 Effects of the hydraulic conductivity anisotropy on the seepage characteristics

264 In accordance with the calculation conditions detailed in Table 3, a total of 28 numerical simulations were
265 carried out, and 84 sections of volumetric water content variations were obtained. Figure 8 shows the changes in
266 the volumetric water content with different values of α when $k_r = 0.01$ and $k_r = 0.1$, respectively. The goal was to
267 illustrate the effects of the anisotropy direction α on the seepage characteristics. In Figure 9, the volumetric water
268 content changes with different values of k_r when $\alpha = -15^\circ$, $\alpha = -45^\circ$ and $\alpha = -90^\circ$ are shown in order to illustrate
269 the effects of the anisotropy ratio k_r on the seepage characteristics. The rainfall infiltration depth (RID) and the
270 maximum surface water content (MWCS) are defined. Figure 11 shows the changes of MWCS and RID of rock
271 slopes with different kr and α .

272 4.2.1 Analysis of the volumetric water content

273 Fig. 7 shows the changes in the volumetric water content of the carbonaceous slate in different regions under
274 the conditions of different anisotropy angle α values. The initial state consisted of the distribution of water content
275 of the slope before the rain, and the remainder was the state of the distribution of water content after the rain had
276 stops.

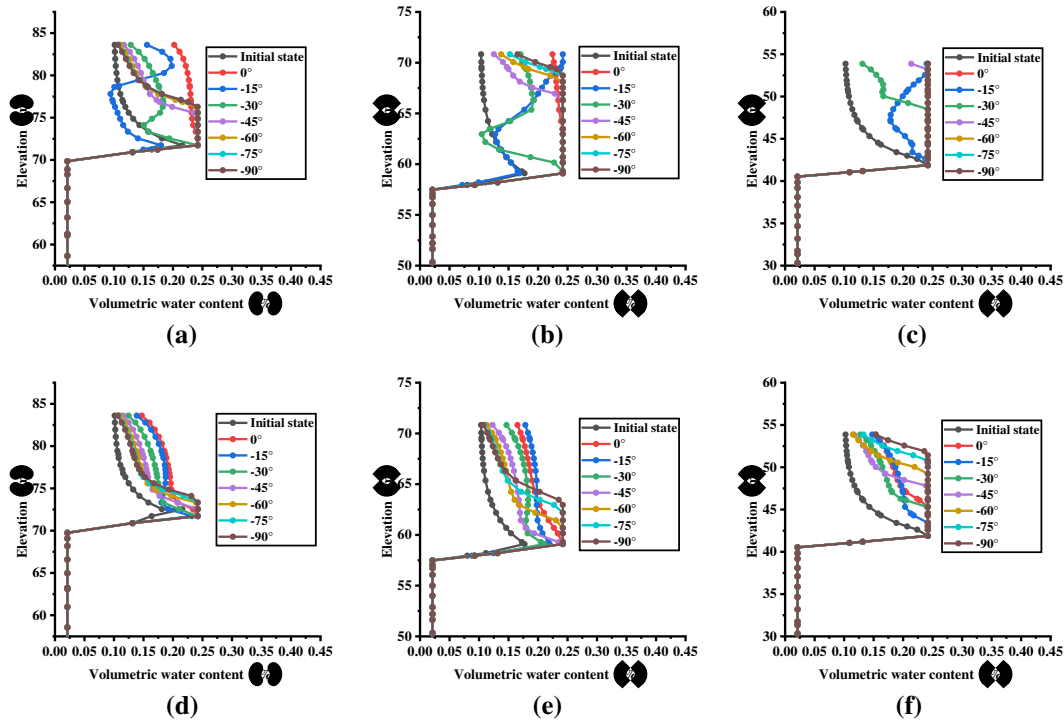
277 From the aspect of the top of the slope, the volumetric water content of the slope surfaces was observed to
278 decrease as the angle α decreased. This was due to the fact that the hydraulic conductivity in the horizontal
279 direction was greater than that in the vertical direction. It was found that when the angle α was equal to 0° , the
280 vertical penetration was the smallest. Subsequently, following rainfall events, rainwater tended to accumulate on
281 the surfaces of the slope. However, with decreases in the angle α , the vertical permeability continuously increased,
282 and the rainwater was more likely to seep into the deeper parts of the slope. It was determined from the comparison
283 results of the different anisotropy ratios that when the anisotropy ratio was larger (for example, $k_r = 0.1$), the

284 influencing effects of the rainfall on the volumetric water content were mainly concentrated on the surfaces of the
 285 slope. In addition, when the anisotropy was relatively small (for example, $k_r = 0.01$), the rainfall not only affected
 286 the volumetric water content of the surfaces, but also strongly affected the volumetric water content of the deeper
 287 parts of the slope, particularly at -15° and -30° .

288 When examining the middle sections of the slope, it was found that the volumetric water content was affected
 289 by both rainfall infiltration and rainfall discharge at the top of the slope. Furthermore, as previously described, as
 290 the angle α decreased, the volumetric water content of the middle sections of the slope gradually decreased.
 291 However, when $\alpha = -15^\circ$, the volumetric water content of the surface area reached the maximum. In addition,
 292 when the anisotropy was relatively small (for example, $k_r = 0.01$), the impacts of the rainfall events on the deeper
 293 parts of the slope were found to be more severe.

294 For the bottom of the slope, when the anisotropy was relatively small (for example, $k_r = 0.01$), the rainfall
 295 was found to have a severe effects on the volumetric water content of the deeper parts of the slope. When the
 296 plane was inclined at -15° or -30° , the volumetric water content levels of the deeper parts of the slope body were
 297 low, which resulted in decreased excretion. As a result, this had led to large changes in the volumetric water
 298 content levels of the surfaces in the bottom of the slope.

299
 300



301
 302
 303
 304
 305

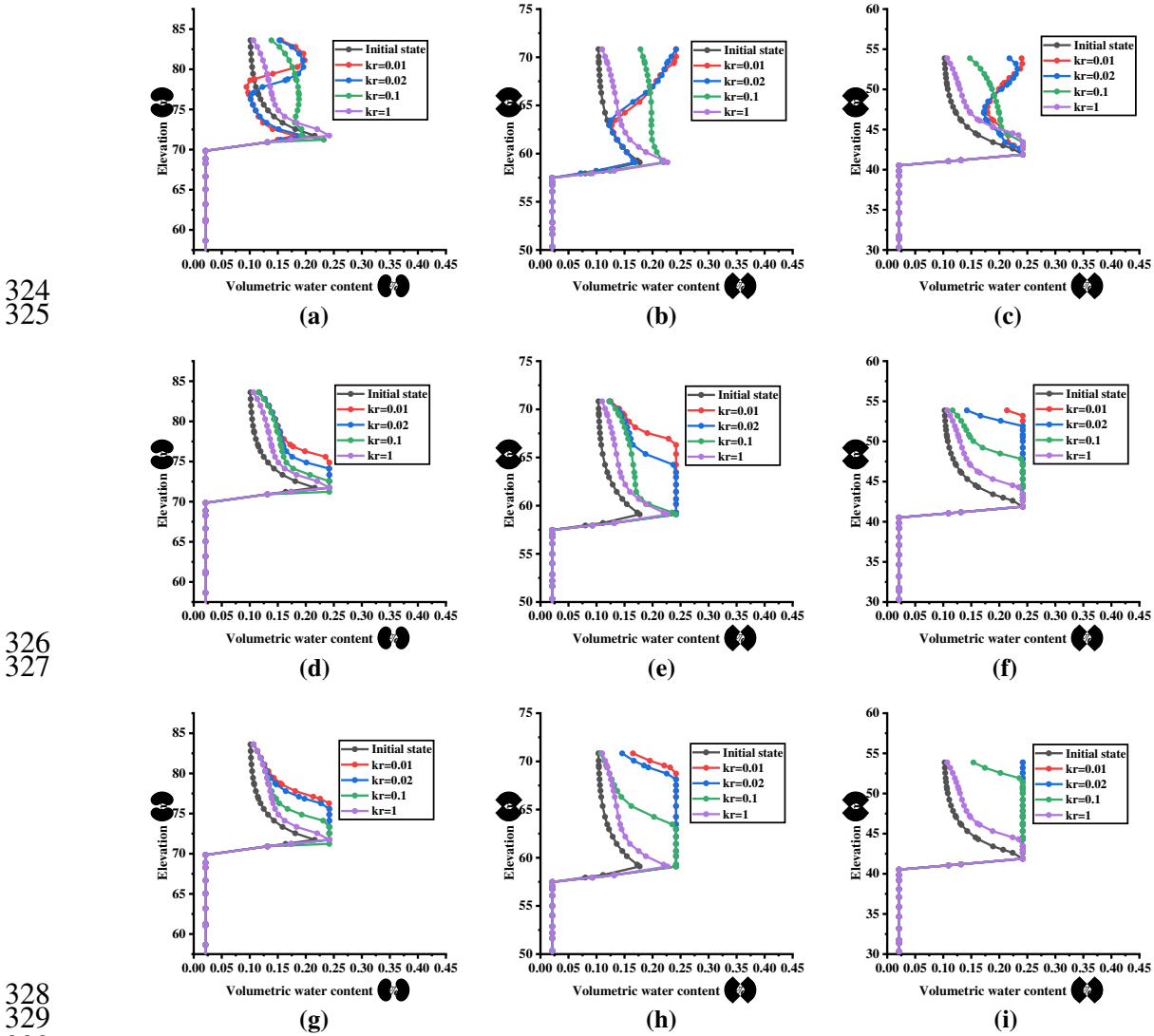
Fig. 7 Variations in the volumetric water content levels under different α values for the anti-dipping carbonaceous slate slopes: **a** Top of the slope with $k_r=0.01$, **b** Middle of the slope with $k_r=0.01$, **c** Bottom of the slope with $k_r =0.01$, **d** Top of the slope with $k_r =0.1$, **e** Middle of the slope with $k_r =0.1$, **f** Bottom of the slope with $k_r =0.1$

306 Fig. 8 shows that the volumetric water content of the slope was affected by the anisotropy ratio k_r . At the top
 307 of the slope, the volumetric water content of the slope surfaces decreased with the increases in the anisotropy ratio
 308 k_r , due to fact that the k_r increases had led to weakening of the horizontal penetration. Consequently, an
 309 accumulation of rainwater on the surfaces of the slope. This study determined from the comparison results of the
 310 different α angles, that when the value of α is small (for example, $\alpha = -15^\circ$), the rainfall had strong influencing
 311 effects on the deeper parts of the slope, particularly at $k_r = 0.01$ and $k_r = 0.02$. The reason for these effects were
 312 related to the fact that when k_r was small, the vertical permeability was reduced, and the rainwater had slowly
 313 seeped into the deeper parts of the slope. This had caused the groundwater levels to rise slowly, forming a negative
 314 pressure zone in the deeper parts of the slope.

315 It was observed that for the middle sections of the slope, the variation range of the volumetric water content
 316 was larger than that of the top sections of the slope. The turning point of the volumetric water content curve
 317 appeared in the deeper parts of the slope. The humidity conditions in the area above those points began to change

318 from saturated to unsaturated, which indicated that the groundwater levels had risen to a turning point after the
 319 rainfall had ceased.

320 In addition, due to terrain problems in the bottom region of the slope, the initial water level was relatively
 321 small. The bottom area of the slope was not only be affected by rainfall, but also by the drainage of rainwater
 322 from the middle section of the slope. Therefore, the speed at which the foot of the slope reached its saturation
 323 point, along with the rising of the groundwater, were faster than in the other sections.



324
325

326
327

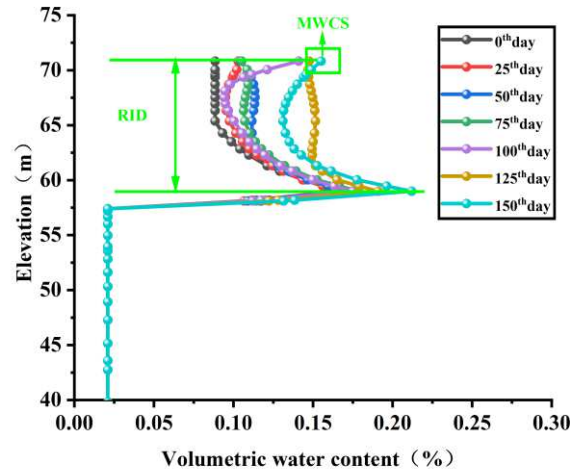
328
329

330 **Fig. 8** Volumetric water content levels at different positions on the anti-dipping carbonaceous slate slope under
 331 different k_r values with $\alpha = -15^\circ$ 、 $\alpha = -30^\circ$ and $\alpha = -45^\circ$: **a** Top of the slope with $\alpha = -15^\circ$, **b** Middle of the slope
 332 with $\alpha = -15^\circ$, **c** Bottom of the slope with $\alpha = -15^\circ$, **d** Top of the slope with $\alpha = -45^\circ$, **e** Middle of the slope with
 333 $\alpha = -45^\circ$, **f** Bottom of the slope with $\alpha = -45^\circ$, **g** Top of the slope with $\alpha = -90^\circ$, **h** Middle of the slope with $\alpha = -$
 334 90° , **i** Bottom of the slope with $\alpha = -90^\circ$.

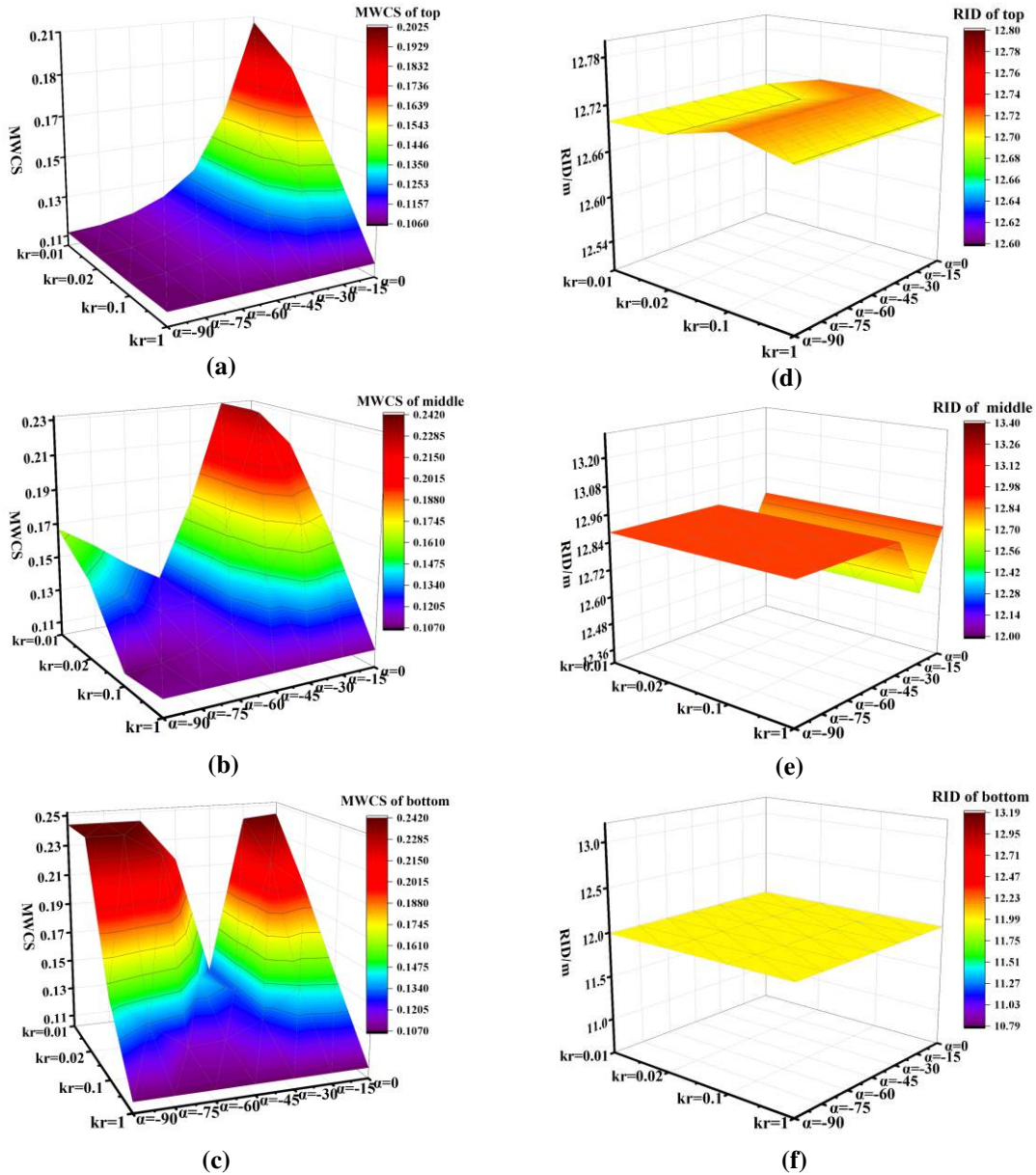
335 *4.2.2 Analysis of the rainfall infiltration depth and maximum surface water content levels*

336 It was concluded from the aforementioned results that the hydraulic conductivity anisotropy ratios k_r and the
 337 anisotropy directions α had major influences on the permeability of the anti-dipping slope. In order to further
 338 study the influencing effects of different k_r and α on the infiltration of rock slopes, the rainfall infiltration depths
 339 (RID) and maximum surface water content (MWCS) levels were defined. As shown in Fig. 9, the volumetric
 340 water content levels on the slope had changed with time. As the rainfall continued, the volumetric water content
 341 levels of the slope gradually increased until the rainfall ended. Therefore, the MWCS was defined in order to
 342 represent the saturation of the slope surfaces, which was the maximum water content of the surfaces after the

343 rainfall had ceased. During the rainfall process, the rainwater had infiltrated into deeper areas of the slope. The
 344 RID was used to express the impacts of the rainfall at a specific depth in the slope. This depth was the height from
 345 the turning point to the slope surfaces. The data detailed in Fig. 9 were taken at the water conductivity anisotropy
 346 $k_r = 0.1$ and $\alpha = -60^\circ$. It can be seen in the figure that for the strongly weathered carbonaceous slate, the rainwater
 347 had easily penetrated the layers, and the differences were large. It should be noted that the volumetric water content
 348 of the deeper slope areas was observed to change drastically at the 100-days and 150-days points. This
 349 was determined to be due to no rainfall occurring for a period of time prior to those timeframes.



350
 351 **Fig. 9** Variations in the volumetric water content levels



352 **Fig. 10** Variations in the MWCS and RID with different k_r and α : **a** MWCS of top of the slope, **b** MWCS of the
 353 middle of the slope, **c** MWCS of the bottom of the slope, **d** RID of top of the slope, **e** RID of middle of the slope,
 354 **f** RID of the bottom of the slope.
 355

356 Fig. 10 details the changes in the MWCS and RID values of the rock slope with different k_r and α . For the
 357 examined anti-dipping carbonaceous slate slope, the MWCS gradually decreased as the k_r increased and the α
 358 decreased. However, when reaching the bottom of the slope, the value of the MWCS was observed to become
 359 larger than those the top and the middle sections of the slope, which indicated that the bottom of the slope was
 360 more likely to reach its saturation point more quickly due to its height during the rainfall. It was also observed
 361 that for the broken center and the bottom of the carbonaceous slate inverted layer, when $\alpha = -45^\circ$ and the k_r was
 362 small, the MWCS tended to have a smaller value. This was attributed to the fact that when $\alpha = -45^\circ$, the slope was
 363 perpendicular, and the infiltration of the slope was consistent with the infiltration in the horizontal direction. In
 364 other words, the surface areas of the slope experienced rainfall in two directions. However, when the anisotropy
 365 angle was greater than -45° , the horizontal infiltration was much larger than the vertical infiltration. In contrast,
 366 when the anisotropy angle was less than -45° , the vertical penetration was much greater than the horizontal
 367 penetration. The maximum values and change rates of the MWCS are shown in Table 5. The change range of the
 368 MWCS at the top of the slope was between 0.1064 and 0.202, and the change rate was 23%. The range of the
 369 MWCS in the middle of the slope was between 0.10733 and 0.23, and the rate of change was 114%. The range of
 370 the MWCS at the middle of the slope was determined to be between 0.10704 and 0.242, and the rate of change

371 was 126%. Therefore, it was found that the change rates of the MWCS were larger in the middle and bottom
 372 sections of the slope, which indicated that the MWCS in the middle and bottom sections of the slope were more
 373 affected by the k_r and α .

374 **Table 5** MWCS maximum and minimum values and rates of change

Slope position	Minimum value of MWCS	Maximum value of MWCS	Rate of change
Top of the slope	0.1064	0.202	23%
Middle of the slope	0.10733	0.230	114%
Bottom of the slope	0.10704	0.242	126%

375 The RID changes of the anti-dipping carbonaceous slate slope are detailed in Fig. 10d, Fig. 10e, and Fig. 10f.
 376 Table 6 shows the maximum values and change rates of the RID. It was found that under different conditions of
 377 k_r and α , the variation range of the slope top RID was between 12.69907 and 12.71925 m, and the variation rate
 378 was 0.16%. The range of the RID in the middle section of the slope was between 12.62164 and 12.88343 m, and
 379 the rate of change was determined to be 2.07%. In addition, the RID at the bottom of the slope was not observed
 380 to change. The RID was 11.99025 m, and the rate of change was 0%. Therefore, this study determined that the
 381 maximum value of the RID appeared in the middle section of the slope, and the minimum value appeared at the
 382 bottom of the slope. The RID in the middle section of the slope had the largest rate of change, which indicated
 383 that the RID in the middle area of the slope was most affected by the k_r and α . Furthermore, it was observed that
 384 the RID change rate at the bottom of the slope was the smallest, which indicated that the RID at the bottom was
 385 the least affected by the k_r and α .

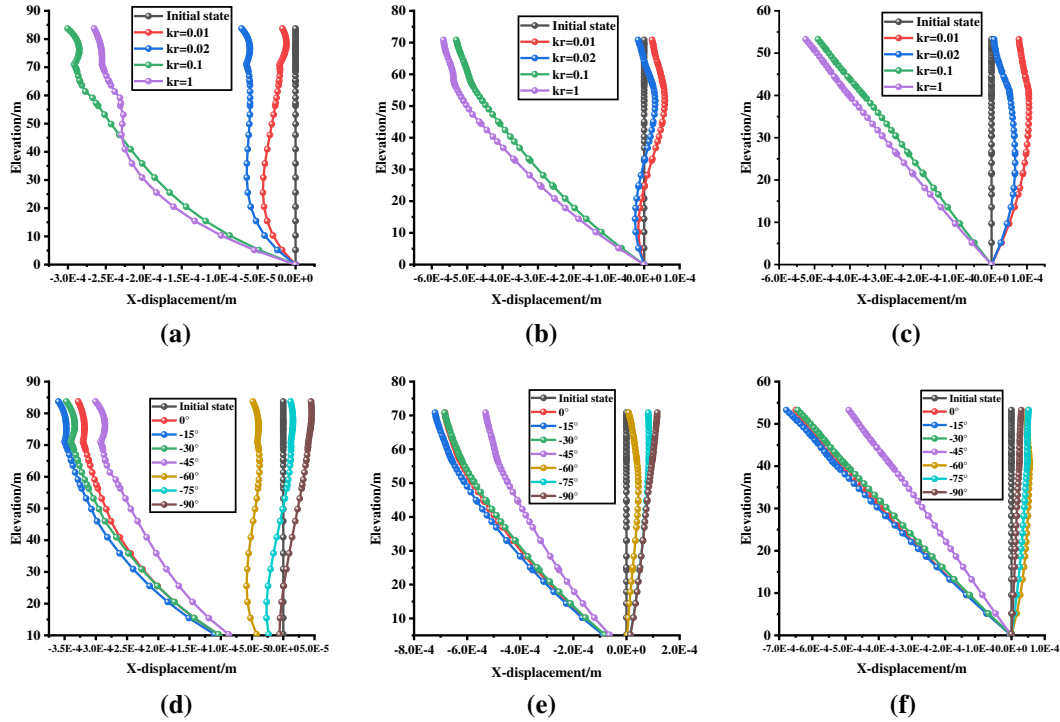
386 **Table 6** RID maximum and minimum values and rates of change

Slope position	Minimum value of RID	Maximum value of RID	Rate of change
Top of the slope	12.69907m	12.71925m	0.16%
Middle of the slope	12.62164m	12.88343m	2.07%
Bottom of the slope	11.99025m	11.99025m	0%

387 4.3 Influencing effects of the hydraulic conductivity anisotropy on the displacements of the anti-dipping slopes

388 In the present study, based on the fluid-solid coupling theory, it was considered that the anti-dipping layered
 389 rock mass would produce corresponding displacements under the action of fluid. In order to highlight the
 390 influencing effects of the anisotropy angles and anisotropy ratios on the horizontal displacements, anisotropy ratio
 391 $k_r = 0.1$ was selected, along with anisotropy angle $\alpha = -45^\circ$. The changes are shown in Fig. 11. The initial state
 392 was the horizontal displacements of the slope when there was no rainfall, and the remainder was the horizontal
 393 displacements when the rainfall stopped. It can be seen in the Fig. 11 that the displacements in the slope and the
 394 slope bottom were relatively large, while the displacements of the slope top were relatively small. Therefore, if
 395 any landslides were to occur in the slope due to rainfall, they would tend to be traction landslides. When α does
 396 not change, then as k_r decreases, there will be differences in the horizontal displacements of the slope. In the top
 397 area of the slope, the horizontal displacements would increase with the increases in elevation, and the horizontal
 398 displacements of the slope could be underestimated in the isotropic state. It was observed in this study that for the
 399 middle and bottom areas of the slope, when $k_r = 0.01$ and $k_r = 0.02$, the horizontal displacements first increased,
 400 and then decreased with the elevation. The maximum displacement was approximately 17 m from the surface.
 401 However, when $k_r = 0.1$ and $k_r = 1$, the horizontal displacements increased with the increase in elevation, and the
 402 maximum displacement was on the slope surface. At that time, the horizontal displacements of the slope could be
 403 overestimated in the isotropic state.

404 It was found in this study that when k_r was constant and the anisotropy angle was less than -45° , the horizontal
 405 displacement produced by the slope were smaller. In addition, when the anisotropy angle was greater than -45° ,
 406 the slope produced larger horizontal displacements, particularly at -15° and -30° . This was due to the fact that the
 407 horizontal permeability in that state was much greater than the permeability in the vertical direction. Also, due to
 408 the existence of elevation difference, the rainwater flowed all the way to the foot of the slope. Therefore, the
 409 horizontal displacements at the bottom of the slope were larger than those at the top and middle sections of the
 410 slope.



411
412

413
414

Fig. 11 Variations in the x-displacement under different kr and α values for anti-dipping carbonaceous slate slopes: a Top of the slope with $\alpha = -45^\circ$, b Middle of the slope with $\alpha = -45^\circ$, c Bottom of the slope with $\alpha = -45^\circ$, d Top of the slope with $kr = 0.1$, e Middle of the slope with $kr = 0.1$, f Bottom of the slope with $kr = 0.1$

418

In the current investigation, for the purpose of quantitative research, the maximum horizontal displacement (MHD) of an anti-dipping carbonaceous slate slope under different anisotropic permeability characteristics, along with the changes in the MHD under different conditions, are detailed in Fig. 12. The influencing effects of the permeability anisotropy on the MHD were found to vary with the slope position (for example, the top, middle, and bottom sections of the slope). The MHD was largest at the foot of the slope, smaller at the middle of the slope, and the smallest at the top of the slope. As shown in Table 7, for the examined anti-dipping carbonaceous slate slope, considering only the top, middle, and bottom of the slope, the differences between the maximum and minimum MHD were 60.9%, 37.8% and 29.8%, respectively. Also, considering the two factors of the kr and α , the differences of the anti-dipping carbonaceous slate slope were 71.4%, 46.3% and 39.7%, respectively. It was found that under the conditions that only the anisotropy ratio kr and the anisotropy ratio kr and the rock formation dip α were considered, the MHD values differed greatly. Therefore, this study determined that in cases of anti-dipping layered rock slopes, both the anisotropy ratios and rock layer dip angles should be considered in deformation analysis.

419

420

421

422

423

424

425

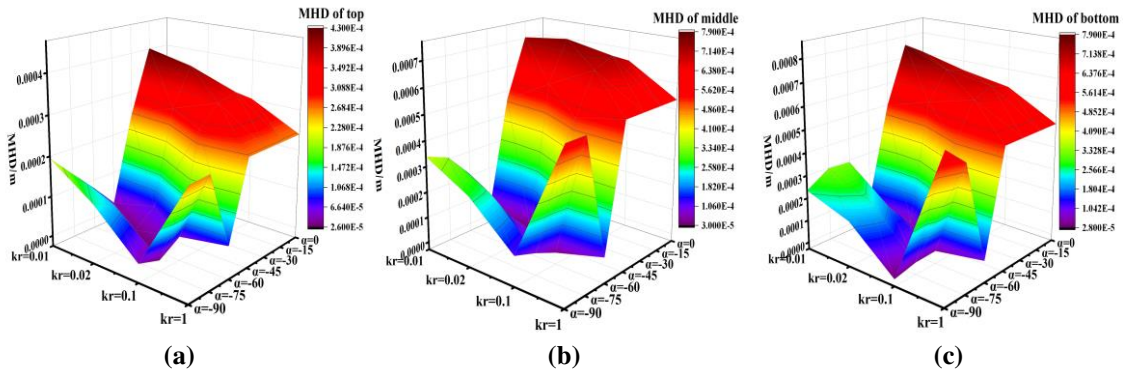
426

427

428

429

430



431

Fig. 12 Variations in the maximum horizontal displacement (MHD) under different kr and α values: a Top of the slope, b Middle of the slope, c Bottom of the slope

433

434

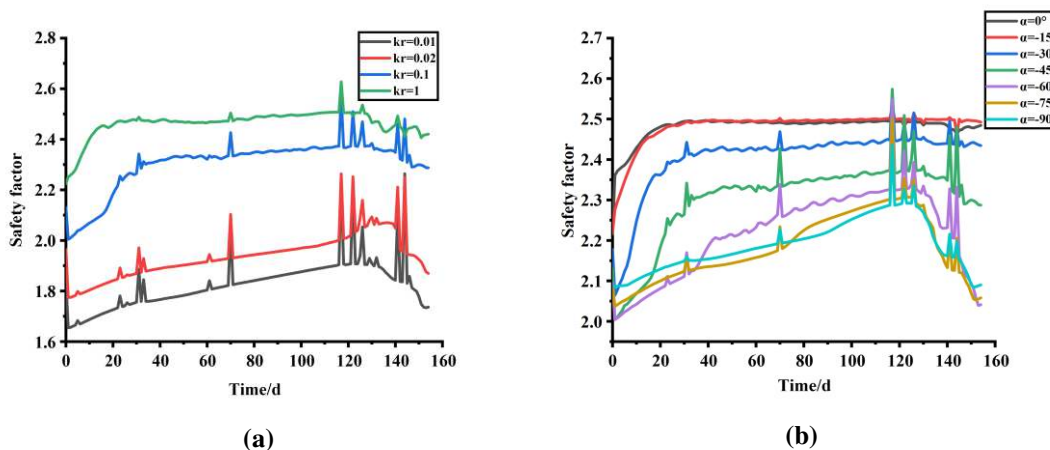
435

Table 7 MHD considering k_r only and considering the differences between the k_r and α

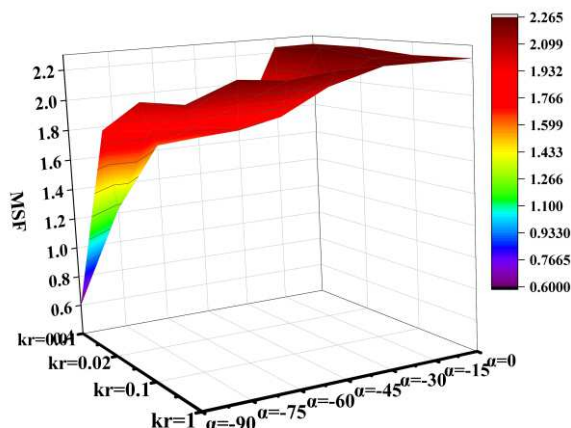
Analysis content		Only Consider k_r	Consider k_r and α
MHD (Top)	Carbonaceous slat slope	60.9%	71.4%
MHD (Middle)	Carbonaceous slat slope	37.8%	46.3%
MHD (Bottom)	Carbonaceous slat slope	29.8%	39.7%

437 4.4 Influencing effects of the anisotropy of hydraulic conductivity on the stability of anti-dipping rock slopes

438 Fig. 13 shows the changes in the safety factors (SF) of a carbonaceous slate slope under different permeability
 439 anisotropy ratios k_r and direction angles α . In order to highlight the influencing effects of the anisotropy angles
 440 and the anisotropy ratios on the safety factors, $\alpha = -45^\circ$ was selected to change the anisotropy ratio k_r , and $k_r = 0.1$
 441 was selected to change the anisotropy angle α . It was found that when α was constant, as k_r decreased, and the
 442 safety factors also gradually decreased. It was also noted that when $k_r = 1$, the safety factor of the slope tended to
 443 be overestimated in the isotropic state. Furthermore, when k_r did not change, as α decreased, the safety factors
 444 also gradually decreased. This was due to the fact that the negative dip angle of the rock formation had increased,
 445 and the permeability of the rock mass increased, as well as the groundwater level, which led to the α decreasing
 446 in soil strength and SF. It was also found that the safety factor curves had fluctuated, as illustrated in Fig. 13. This
 447 was attributed to the fluctuation intervals during the heavy rain events in the area. Following the heavy rain, the
 448 rainwater infiltrated and accumulated on the surfaces of the slope, forming a very large unsaturated zone. The
 449 back pressure impacted the soil body reinforcement. However, after a period of rain, the safety factors of the slope
 450 returned to a stabilized state.



451 **Fig. 13** Variations in the safety factors under different k_r and α values for anti-dipping carbonaceous slate slope:
 452 **a** Slope with $\alpha = -45^\circ$, **b** Slope with $k_r = 0.1$
 453



454 **Fig. 14** Variations in the SF for anti-dipping carbonaceous slate slopes
 455

456 The changes of MSF under different conditions are shown in Fig. 14. It can be seen in the figure that as the
 457 k_r and α decreased, the MSF dropped to a minimum. As detailed in Table 8, when considering only the k_r , the
 458 differences between the maximum and minimum MSF was 70.4% for the carbonaceous slate slope. However,
 459 considering the two conditions of k_r and α , the difference of the carbonaceous slate slope was 77.2%. It can be
 460 found that under the conditions in which only the anisotropy ratios k_r were considered, and under the conditions
 461 in which the anisotropy ratios k_r and the rock inclination angle α were both considered, the MSF values differed
 462 greatly. Therefore, for anti-dipping layered rock slopes, it is recommended that both the anisotropy ratios and rock
 463 layer dip angles are considered in stability analysis processes.

464 **Table 8** MSF only considers the k_r and considers the differences between the k_r and α

	Analysis content	Only Consider k_r	Consider k_r and α
MSF	Carbonaceous slate slope	70.4%	77.2%

465 5. Conclusions

466 This research investigation considered the influencing effects of different anisotropy ratios and the hydraulic
 467 conductivity of the anisotropy angles, and numerically simulated the seepage characteristics, deformations and
 468 stability levels of the an anti-dipping layered carbonaceous slate slope in the Pulang area, of southwestern China.
 469 The research results were as follows:

- 470 (1) The initial conditions was very important for the subsequent calculations of the unsaturated seepage of the
 471 anti-dipping layered rock slope. This study verified that the maximum initial matrix suction of -75 kPa
 472 carbonaceous slate could be selected for the numerical simulations, which was consistent with the actual
 473 situation.
- 474 (2) The anisotropy ratios of the bedding plane and the inclination angles of the strata had major influences on
 475 the seepage of the anti-dipping layered rock slope.
- 476 (3) The maximum surface water content (MWCS) levels and the rainfall infiltration depths (RID) were defined
 477 in order to characterize the seepage characteristics of anti-dipping layered rock slopes. The MWCS gradually
 478 decreased with the increases in the bedding plane anisotropy ratios and the decreases of the anisotropy dip
 479 angles. The MWCS at the bottom of the slope was greatly affected by the anisotropy ratios and the dip angles
 480 of the rock formation. Meanwhile, the RID was found to be less affected by the anisotropy ratios and the dip
 481 angles of the rock formation.
- 482 (4) The permeability anisotropy had a greater impact on the deformations and stability of the anti-dipping
 483 layered rock slope. Under the conditions that only the anisotropy ratios were considered, as well as under
 484 the conditions that both the anisotropy ratios and the dip angles of the formation were considered, the MHD
 485 and MSF values were quite different. Therefore, for anti-dipping layered rock slopes, both the anisotropy
 486 ratios and rock layer dip angles should be considered in deformation and stability analysis processes.
- 487 (5) The safety factors (SF) of slopes tend to be overestimated when the seepage of an anti-dipping layered slope
 488 is considered to be isotropic. With the decreases of the anisotropy ratios and the increases of the inverse tilt
 489 angles of the layered plane, the SF of the examined slope had gradually decreased. However, when the
 490 inclination of an inverted layer plane of a rock slope is large, greater protection measures were required for
 491 the slope.

492 Data Availability

493 The datasets used or analyzed during the current study are available from the corresponding author on reasonable
 494 request.

495 Conflicts of Interest

496 The authors declare that they have no conflicts of interest.

497 Author Contributions

498 Guangkeng Zhang wrote the manuscript, completed the experiment and method design, analyzed the data, and
 499 performed the experiments. Guanyin Lu and Chengzhi Xia helped provide analysis of raw data. Lianrong Wu
 500 and Zongming Xu helped polish the manuscript. Guanyin Lu provided research funding. Ying Bai and Jialu Li
 501 changed the format of the manuscript. All authors have read and agreed to the published version of the manuscript.

502 **Acknowledgments**

503 The authors gratefully acknowledge the finances support provided by The National Natural Science Fund (grant
504 no. 41974148).

505 **Funding**

506 This research was funded by the National Natural Science Foundation of China, grant number 41974148, Hunan
507 Provincial Key Research and Development Program, grant number 2020SK2135, Science and Technology
508 Progress and Innovation Project of Transport Department of Hunan Province, grant number 202012 and Zhejiang
509 2020 Transportation Science and Technology Plan Project, grant number 2020041. The APC was funded by
510 41974148.

511 **References**

- 512 Brooks RH, Corey AT(1964) Hydrology and Water Resources Program: Fort Collins, Colo. Hydraulic Properties
513 of Porous Media
- 514 Cheng HL, Huang C, Weng MC(2019) Failure mechanism of a mudstone slope embedded with steep anti-dip
515 layered sandstones: case of the 2016 Yanchao catastrophic landslide in Taiwan. *Landslides* 40(11):2233-
516 2245
- 517 Chen YF, Yu H, Ma HZ et al(2020) Inverse modeling of saturated-unsaturated flow in site-scale fractured rocks
518 using the continuum approach: A case study at Baihetan dam site, Southwest China. *J. Hydrol* 584:124693-
519
- 519 Cheng DX, Liu DA, Ding EB et al(2005) Analysis on influential factors and toppling conditions of toppling
520 rock slope. *Chinese Journal Geotechnical Engineering* 27(11):127-131
- 521 Calgary AB Canada(2010) GEO-SLOPE International Ltd. Seepage Modeling with SEEP/W 2007: 1-207
- 522 Dakshanamurthy VFDC, Rahardjo H(1987) Coupled tedimensional colidation theory of unsaturated porous
523 media Proceedings of the Fith Intenational Conference on Expansive Soils. Adelaide 99-103
- 524 Fredlund DG, Xing AQ(1994) A structure for deoxyribose nucleic acid. *Canadian Geotechnical Journal*
525 31(4):521-532
- 526 Gan YD, Jia YW, Wang K et al(2015) Rainfall infiltration model of layered soil considering air resistance.
527 *Journal of Hydraulic Engineering* 46(2):164-173 (**in Chinese**)
- 528 Genuchten VTM(1980) A Closed-form Equation for Predicting the Hydraulic Conductivity of Unsaturated
529 Soils1. *Soil Science Society of America Journal* 44(5):892-898
- 530 Huang YL, Qian JF, Li XH et al(2019) Stability Analysis of Anti-toppling Rock Slope. *Bulletin of science and*
531 *technology* 35(3):181-186 (**in Chinese**)
- 532 Iverson RM(2000) Landslide triggering by rain infiltration. *Water Resources Research* 36(7):1897-1910
- 533 Kulatilake PHSW, Malama B, Wang WL(2001) Physical and particle flow modeling of jointed rock block
534 behavior under uniaxial loading. *International Journal of Rock Mechanics and Mining Sciences* 38(5):641-
535 657
- 536 Liu CZ, Chen HQ, Han B, Chen H(2010) Technical support system of emergency response for serious geo-
537 hazards. *Geological Bulletin of China* 29(1):147-156 (**in Chinese**)
- 538 Liu X, Shen YP, Zhang P et al(2020) Deformation characteristics of anti-dip rock slope controlled by
539 discontinuities: a case study. *Bulletin of Engineering Geology and the Environment*:1-11
- 540 Morgenstern NR, Price VE(1965) The Analysis of the Stability of General Slip Surfaces. *Géotechnique*
541 15(1):79-93

542 Mualem Y(1976) A new model for predicting the hydraulic conductivity of unsaturated porous media. *Water*
543 *Resources Research* 12(3):513-522

544 Ning S, Zhuang Y, Tan YZ, Dong DX(2021) Stability Analysis of Anti-slide Pile Slope Considering Soil
545 Anisotrop. *J of China Three Gorges Univ.(Natural Sciences)* 43(1):43-47 (**in Chinese**)

546 Song YQ, Chao CJ, Ye GL(2018) Permeability and anisotropy of upper Shanghai clays. *Rock Soil Mech*
547 39(6):2139-2144

548 Su LH, Li W, Ling N(2012) Study on losing stability mechanism of flare rock slopes—A case study of the left
549 bank slope Jingping first-stage hydropower station. *Sichuan Building Science* 38(1):109-144 (**in Chinese**)

550 Tao ZG, Yu YF, Shi GC, Sun YH(2020) Comprehensive Engineering Geological Analysis on Large-Scale Anti-
551 dip Slopes: A Case Study of Changshanhao Opencast Gold Mine in China. *Geotechnical and Geological*
552 *Engineering*:1-20

553 Xiao YY, Li AR(2020) Change of Soft Rock Slope Stability with Weak Interlayer under Rainfall Conditions.
554 *Journal of Yibin University* 20(12):16-19 (**in Chinese**)

555 Xia CZ, Lu GY, Bai DX(2020) Sensitivity Analyses of the Seepage and Stability of Layered Rock Slope Based
556 on the Anisotropy of Hydraulic Conductivity: A Case Study in the Pulang Region of Southwestern China.
557 *Water* 12(8):2314

558 Yang P, Yang J(2015) Rainfall threshold surface for slopes stability considering antecedent rainfall. *Rock and*
559 *Soil Mechanics* 36(1):169-174 (**in Chinese**)

560 Yang ZY, Chen JM, Huang TH(1998) Effect of joint sets on the strength and deformation of rock mass models.
561 *International Journal of Rock Mechanics and Mining Sciences* 35(1):75-84

562 Yeh PT, Lee KZ, Chang KT(2020) 3D Effects of permeability and strength anisotropy on the stability of weakly
563 cemented rock slopes subjected to rainfall infiltration. *Engineering Geology* 266:105459

564 Yu SY, Ren XH, Zhang JX(2020) Sensibility Analysis of the Hydraulic Conductivity Anisotropy on Seepage
565 and Stability of Sandy and Clayey Slope. *Water* 12(1):277

566 Yao Y, Zhang GC, Chen HJ et al(2020) Study on the failure mechanism of rock slope with layered cataclastic
567 structure. *Chinese Journal of Rock Mechanics and Engineering* 40(X):1-16 (**in Chinese**)

568 Yu SY, Ren XH, Zhang JX et al(2020) Seepage, Deformation and Stability Analysis of Sandy and Clay Slopes
569 with Different Permeability Anisotropy Characteristics Affected by Reservoir Water Level Fluctuations.
570 *Water* 12(1):201

571 Zhong DH, An N, Li MC(2007) 3D dynamic simulation and analysis of slope instability of reservoir banks.
572 *Chinese Journal of Rock Mechanics and Engineering* 26(2):360-367 (**in Chinese**)

573 Zhang GR, Yin KL, Liu LL et al(2005) A real-time regional geological hazard warning system in terms of
574 WEBGIS and rainfall. *Rock and Soil Mechanics* 26(8):1312-1317 (**in Chinese**)

575 Zhang J, Han TC, Dou HQ, Ma SG(2014) Stability of loess slope considering infiltration zonation. *Journal of*
576 *Central South University (Science and Technology)* 45(12):4355-4361 (**in Chinese**)

577 Zhou WH, Yang YY(1990) A structure for deoxyribose nucleic acid. *Journal of Hydraulic Engineering*
578 46(11):48-54 (**in Chinese**)

579 Zhu WS, Zhang G(1994) Sensitivity analysis of the influence of jointed rock mass parameters on surrounding
580 rock damage zone. *Underground Space* 14(1):10-15 (**in Chinese**)

581 Zhu C, He CM, Karakus M(2020) Investigating Toppling Failure Mechanism of Anti-dip Layered Slope due to
582 Excavation by Physical Modelling. Rock Mechanics and Rock Engineering 53(10):1-22

Figures

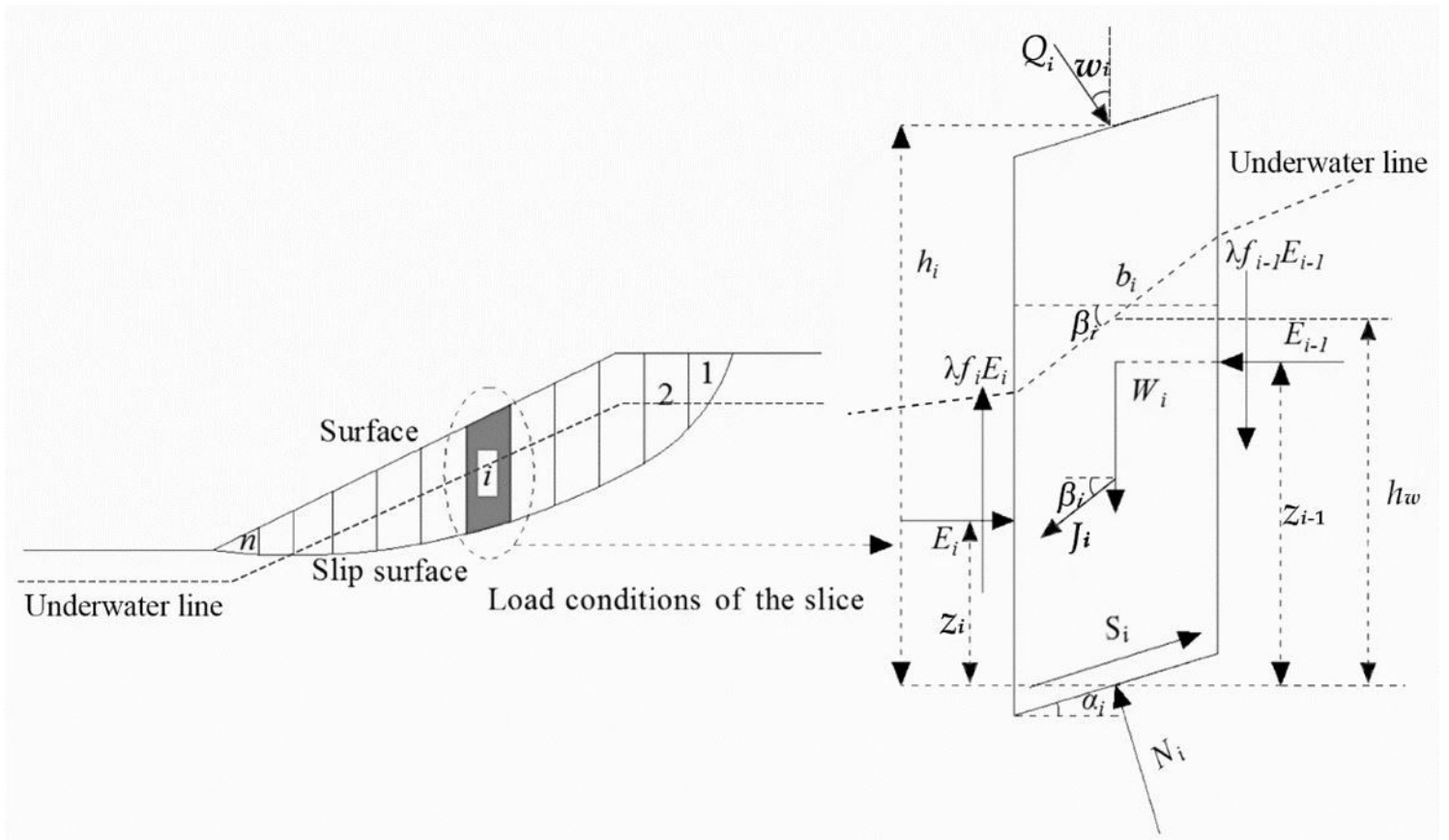


Figure 1

Calculation principle and model of the Morgenstern-Price (M-P) Method

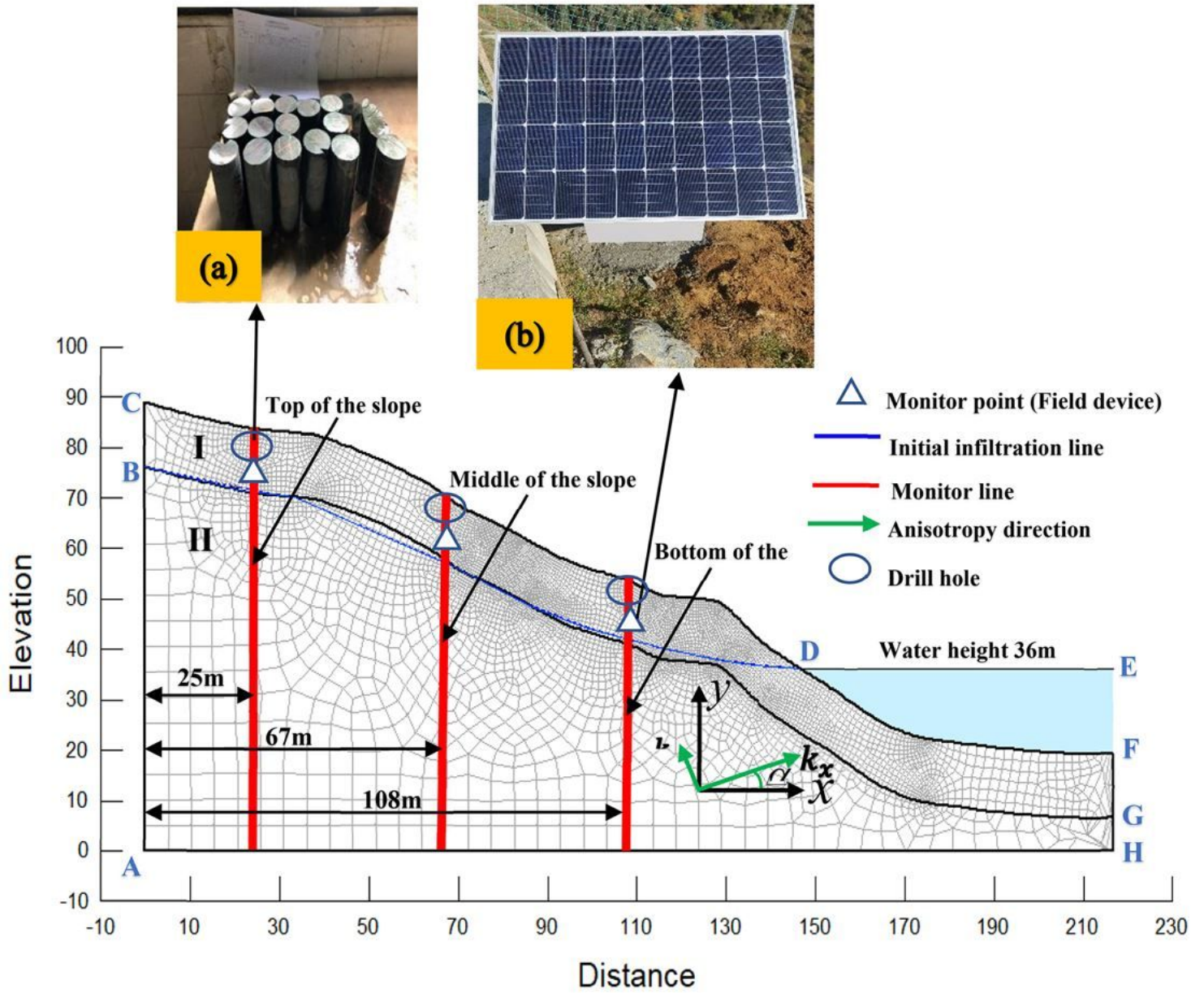


Figure 2

Grid model

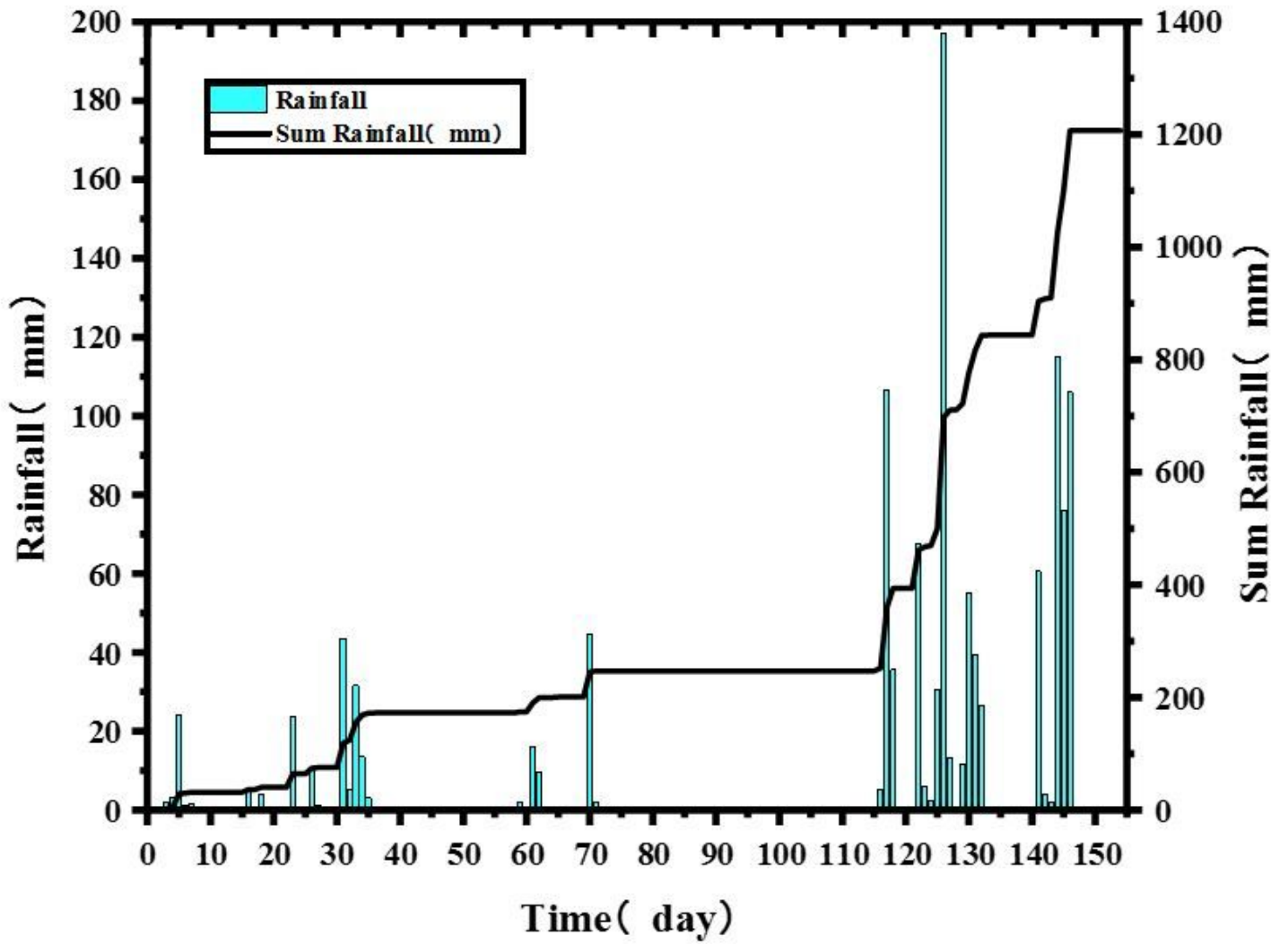


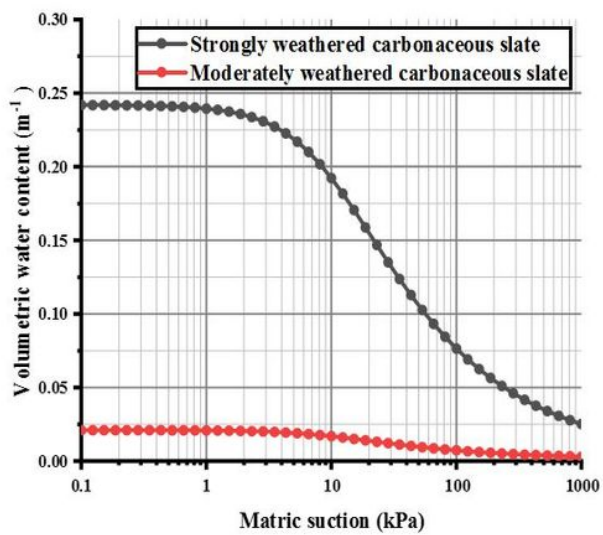
Figure 3

Daily rainfall values from March 1st to August 1st of 2019

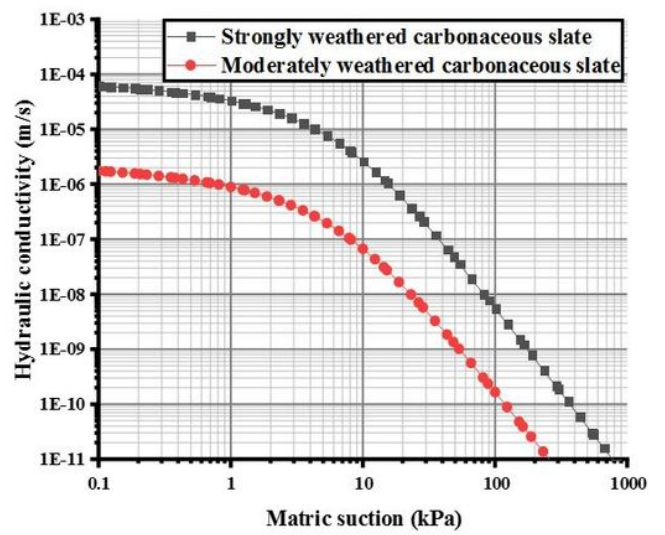


Figure 4

Images of the carbonaceous slate samples



(a)



(b)

Figure 5

SWCC curve: a Water retention curve; b Hydraulic conductivity curve.

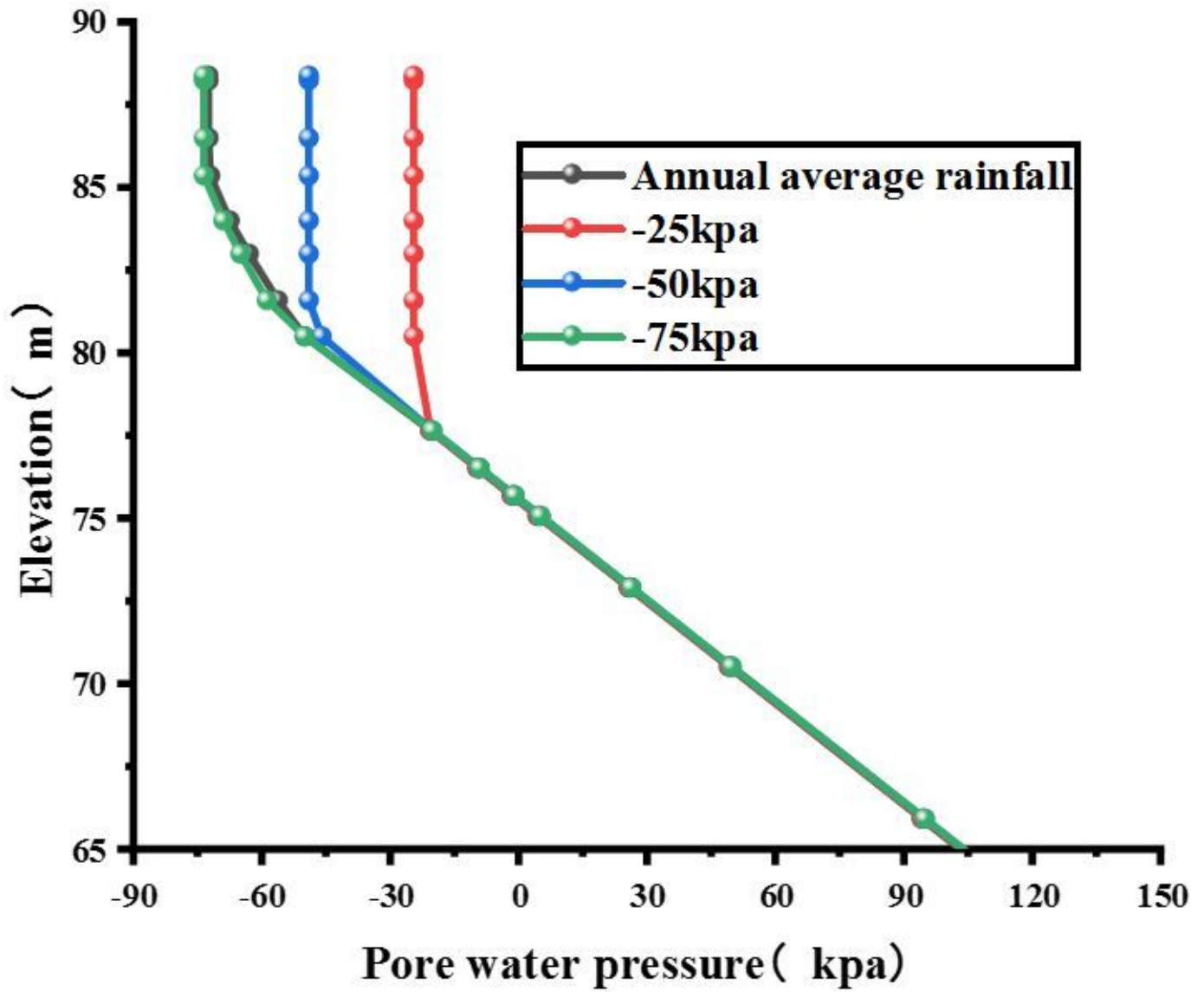


Figure 6

Initial pore pressure distribution

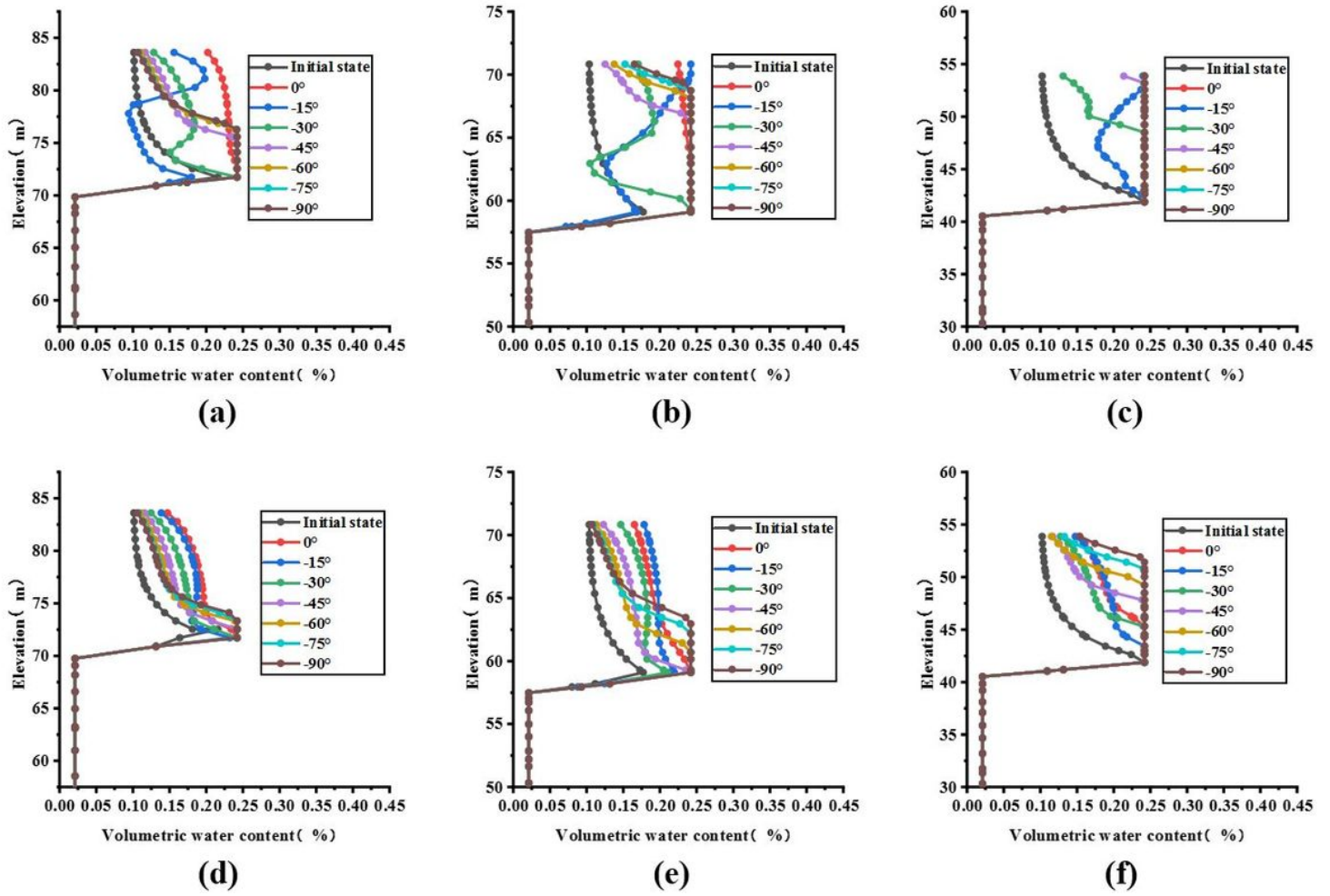


Figure 7

Variations in the volumetric water content levels under different α values for the anti-dipping carbonaceous slate slopes: a Top of the slope with $kr=0.01$, b Middle of the slope with $kr=0.01$, c Bottom of the slope with $kr=0.01$, d Top of the slope with $kr=0.1$, e Middle of the slope with $kr=0.1$, f Bottom of the slope with $kr=0.1$

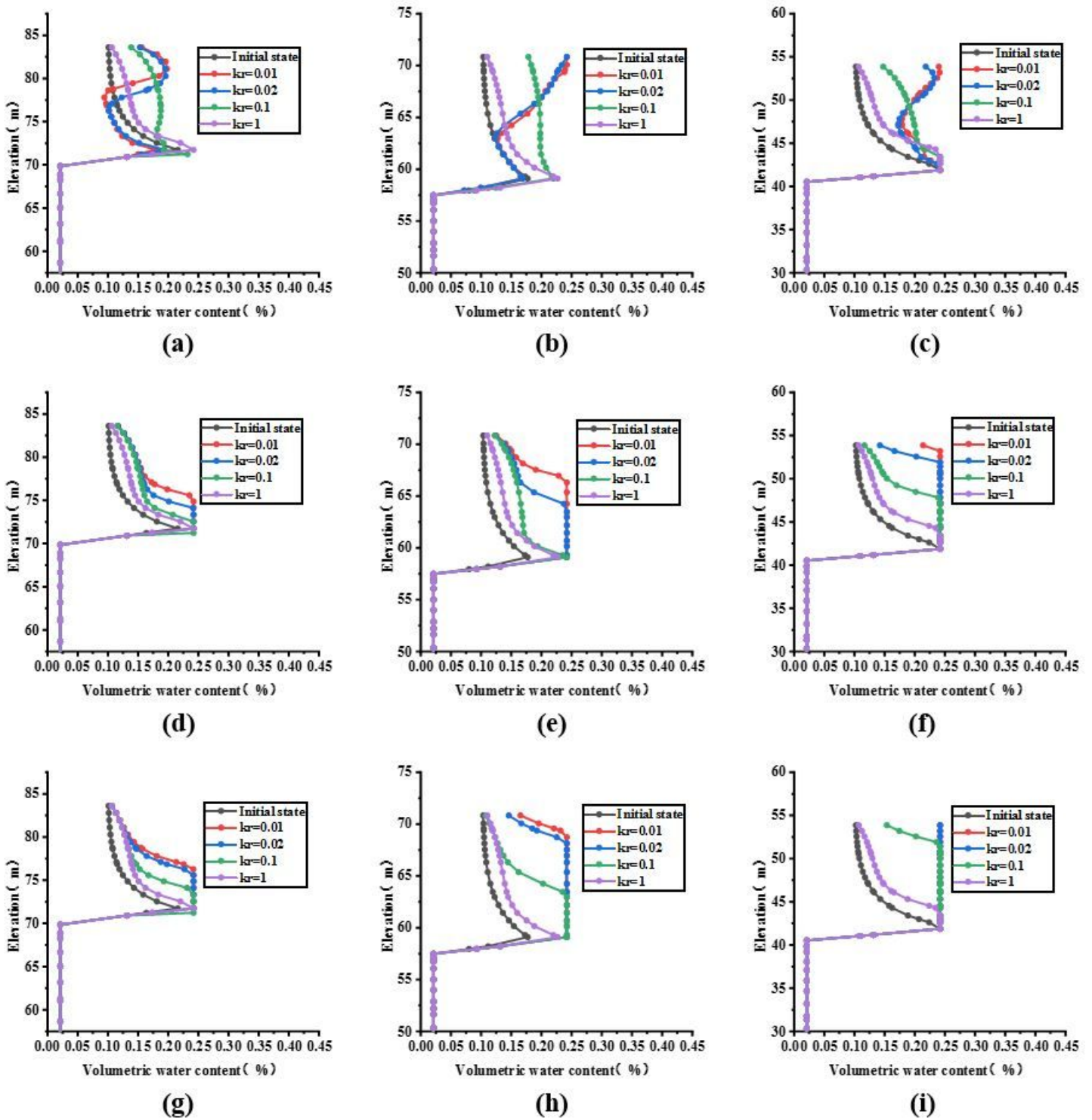


Figure 8

Volumetric water content levels at different positions on the anti-dipping carbonaceous slate slope under different k_r values with $\alpha = -15^\circ$, $\alpha = -30^\circ$ and $\alpha = -45^\circ$: a Top of the slope with $\alpha = -15^\circ$, b Middle of the slope with $\alpha = -15^\circ$, c Bottom of the slope with $\alpha = -15^\circ$, d Top of the slope with $\alpha = -45^\circ$, e Middle of the slope with $\alpha = -45^\circ$, f Bottom of the slope with $\alpha = -45^\circ$, g Top of the slope with $\alpha = -90^\circ$, h Middle of the slope with $\alpha = -90^\circ$, i Bottom of the slope with $\alpha = -90^\circ$.

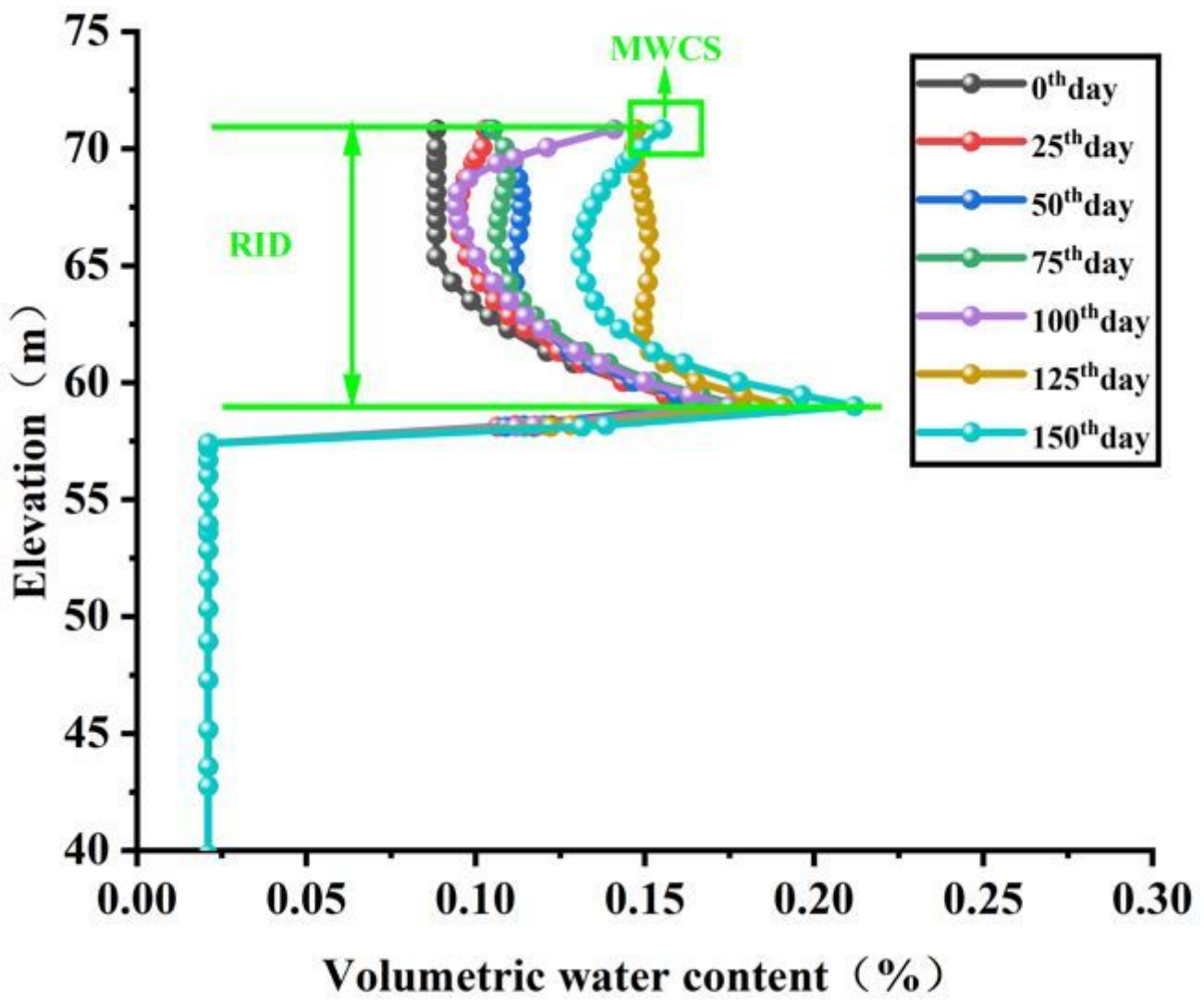
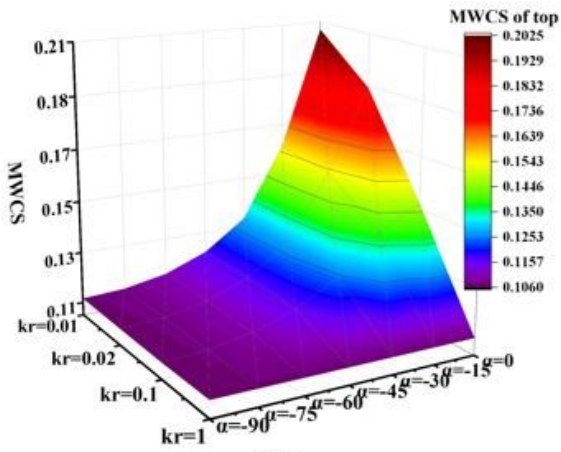
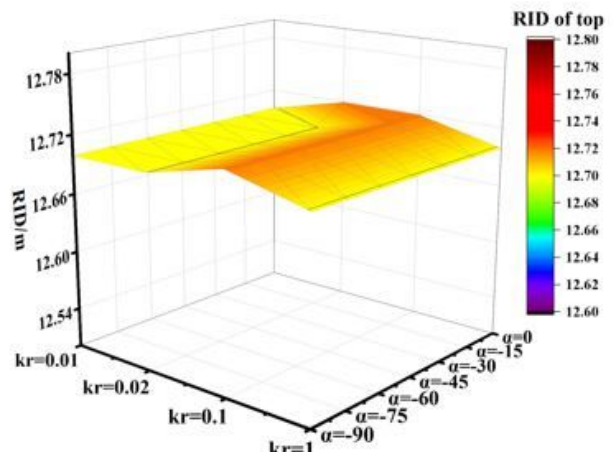


Figure 9

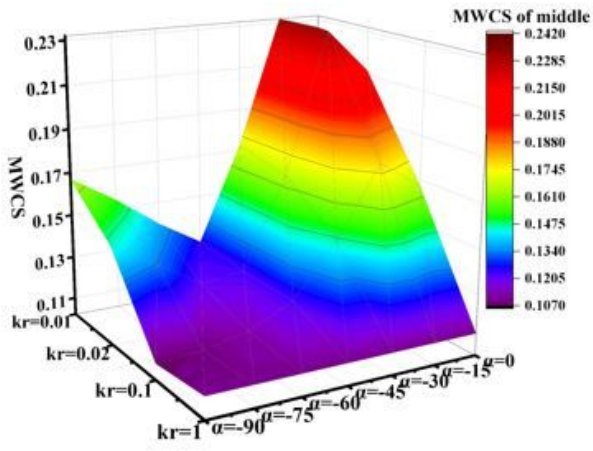
Variations in the volumetric water content levels



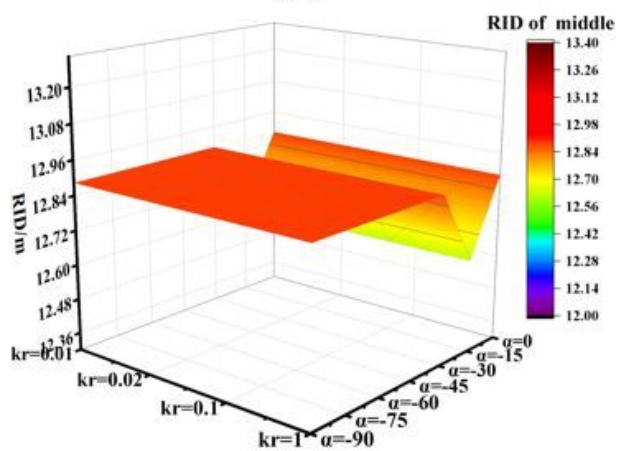
(a)



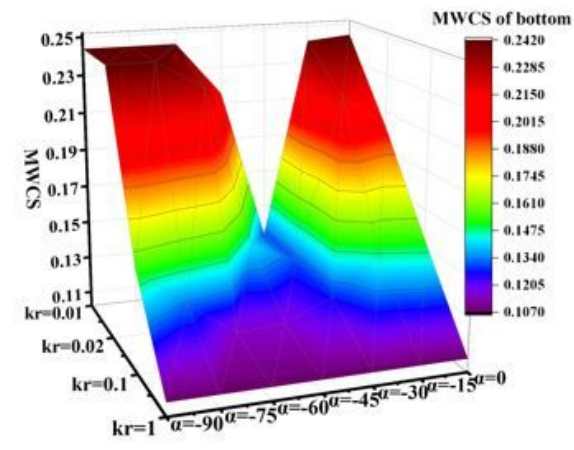
(d)



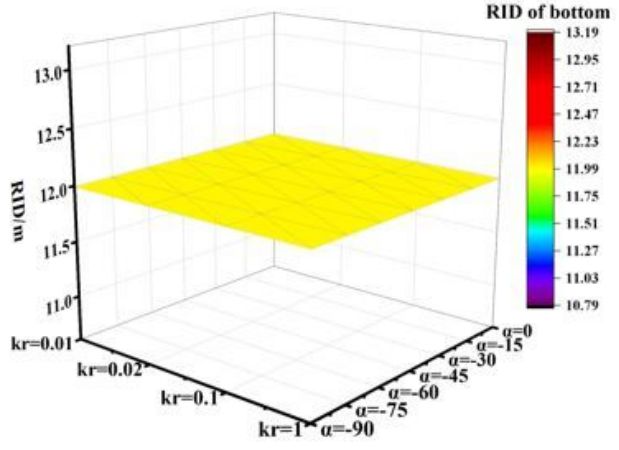
(b)



(e)



(c)



(f)

Figure 10

Variations in the MWCS and RID with different kr and α : a MWCS of top of the slope, b MWCS of the middle of the slope, c MWCS of the bottom of the slope, d RID of top of the slope, e RID of middle of the slope, f RID of the bottom of the slope.

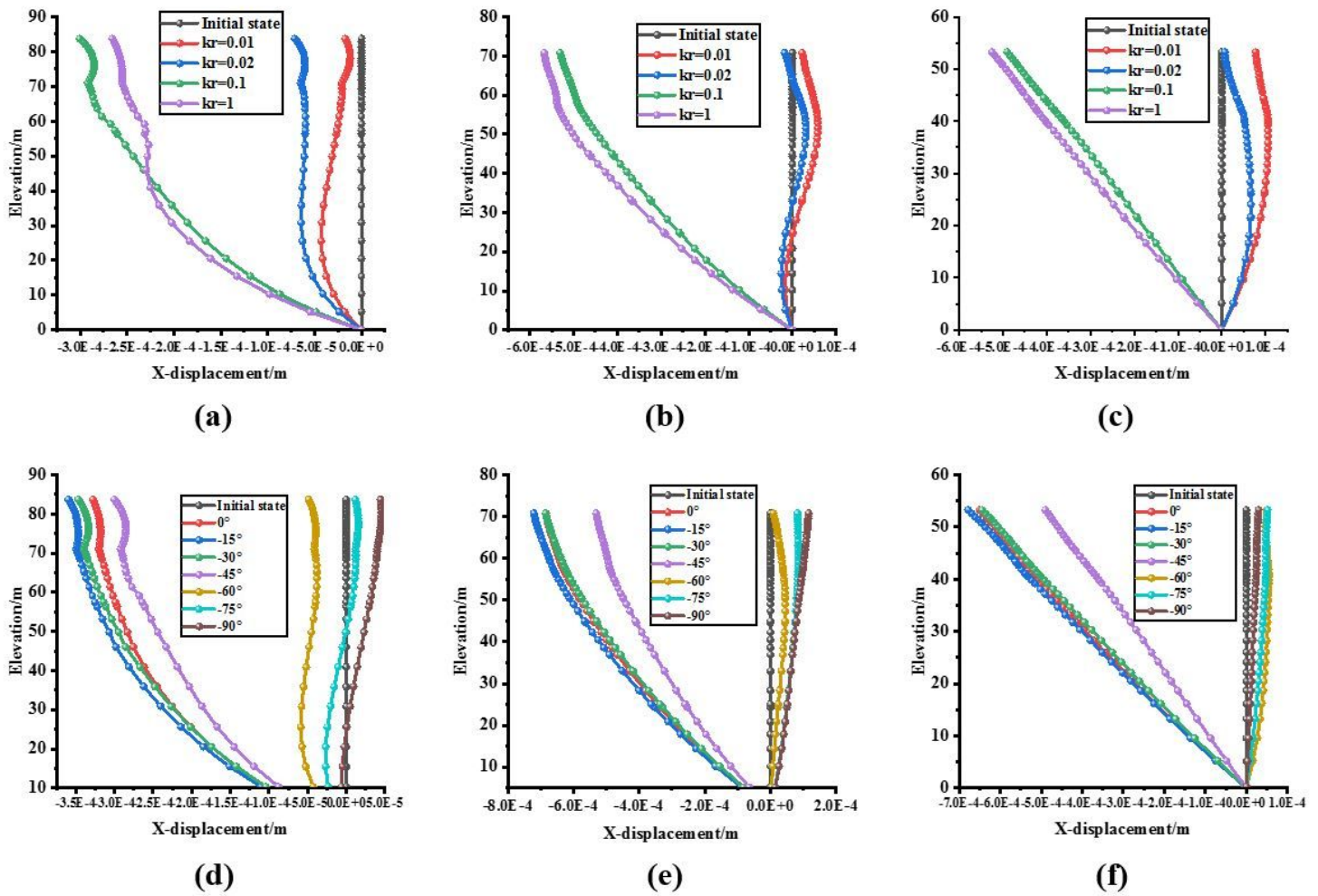


Figure 11

Variations in the x-displacement under different kr and α values for anti-dipping carbonaceous slate slopes: a Top of the slope with $\alpha = -45^\circ$, b Middle of the slope with $\alpha = -45^\circ$, c Bottom of the slope with $\alpha = -45^\circ$, d Top of the slope with $kr = 0.1$, e Middle of the slope with $kr = 0.1$, f Bottom of the slope with $kr = 0.1$

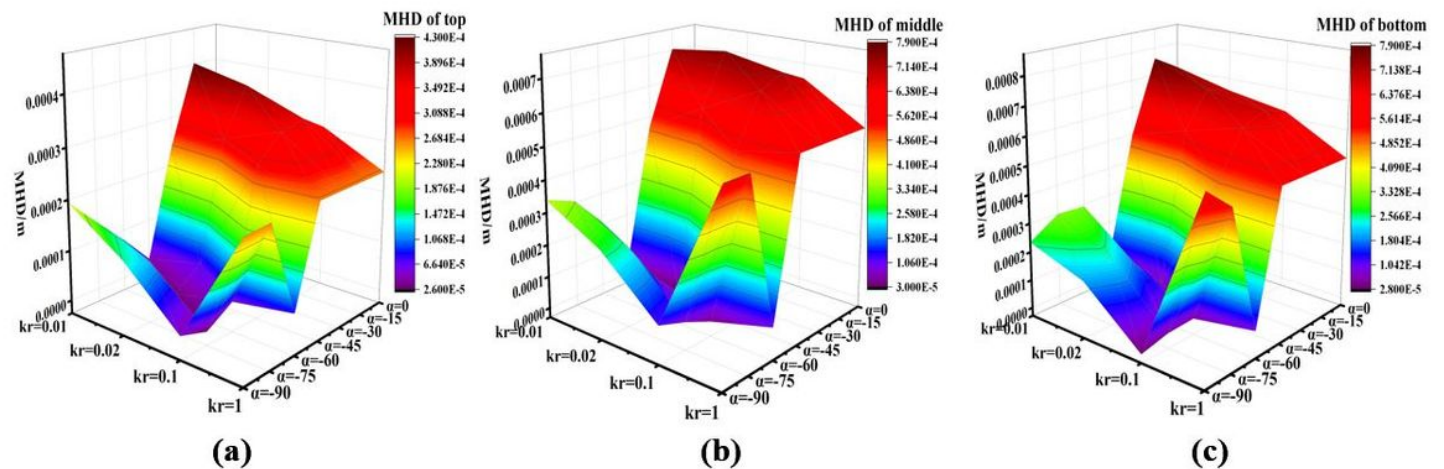


Figure 12

Variations in the maximum horizontal displacement (MHD) under different kr and α values: a Top of the slope, b Middle of the slope, c Bottom of the slope

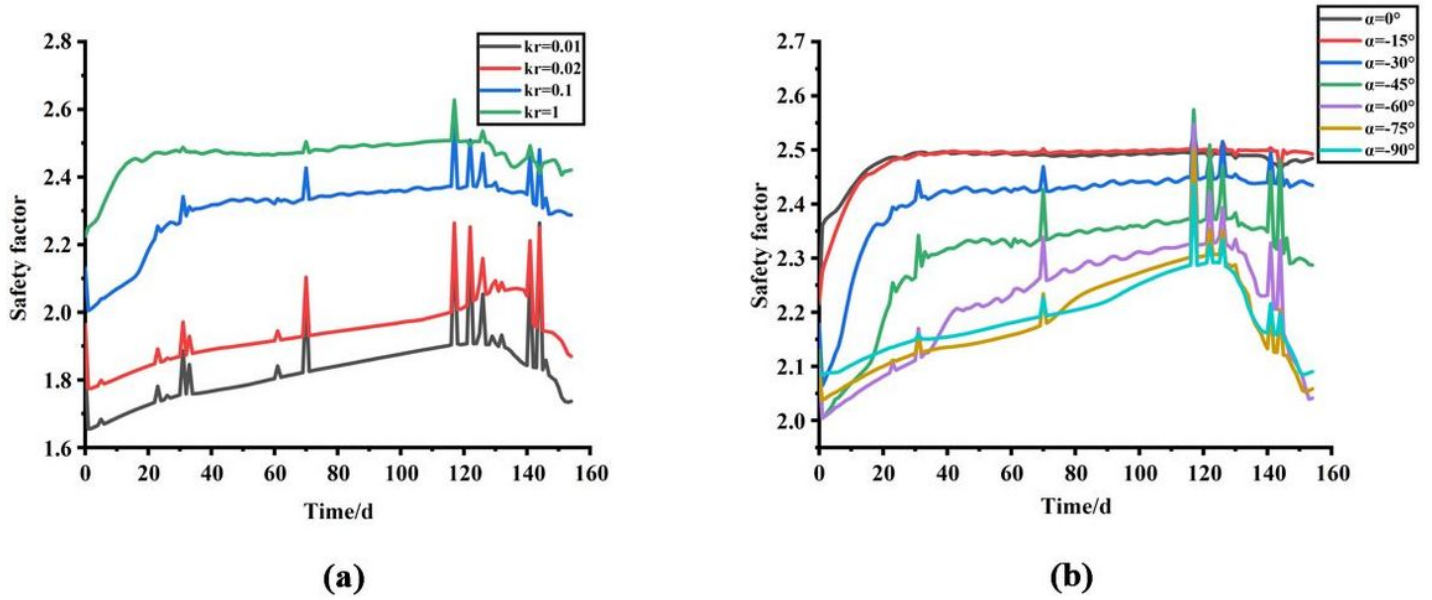


Figure 13

Variations in the safety factors under different kr and α values for anti-dipping carbonaceous slate slope: a Slope with $\alpha = -45^\circ$, b Slope with $kr = 0.1$

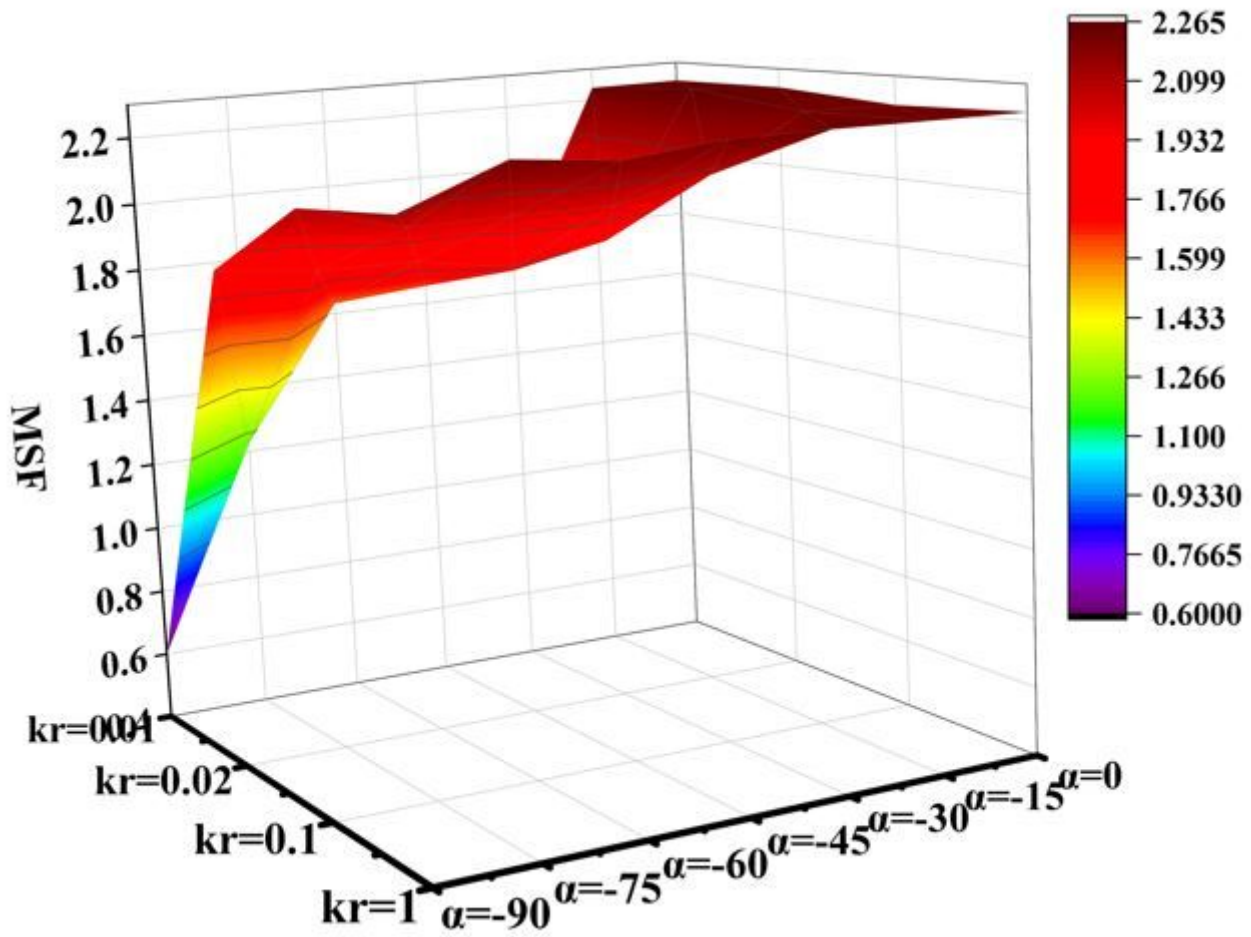


Figure 14

Variations in the SF for anti-dipping carbonaceous slate slopes